Nano Research

ISSN 1998-0124 CN 11-5974/O4
https://doi.org/10.26599/NR.2026.94908891

Research Article

# Metallic states of $Pt/CeO_2$ catalysts dictate the activity for CO oxidation

Sunpei Hu[1,§], Haofan Lei[1,§], Fenglin Peng[1,§], Zizhen Xiao[1], Wenlong Wu[2], Han Yan[1](✉), Chao Ma[3](✉), Jie Zeng[1,2,4](✉)

[1] Hefei National Research Center for Physical Sciences at the Microscale, Key Laboratory of Strongly-Coupled Quantum Matter Physics of Chinese Academy of Sciences, Key Laboratory of Surface and Interface Chemistry and Energy Catalysis of Anhui Higher Education Institutes, Department of Chemical Physics, University of Science and Technology of China, Hefei 230026, China

[2] School of Chemistry & Chemical Engineering, Anhui University of Technology, Ma'anshan 243002, China

[3] College of Materials Science and Engineering, Hunan University, Changsha 410082, China

[4] Deep Space Exploration Laboratory, Hefei 230088, China

[§] Sunpei Hu, Haofan Lei, and Fenglin Peng contributed equally to this work.

*Nano Res.*, **Just Accepted Manuscript** • https://doi.org/10.26599/NR.2026.94908891

**https://www.sciopen.com/journal/1998-0124** on May. 27, 2026

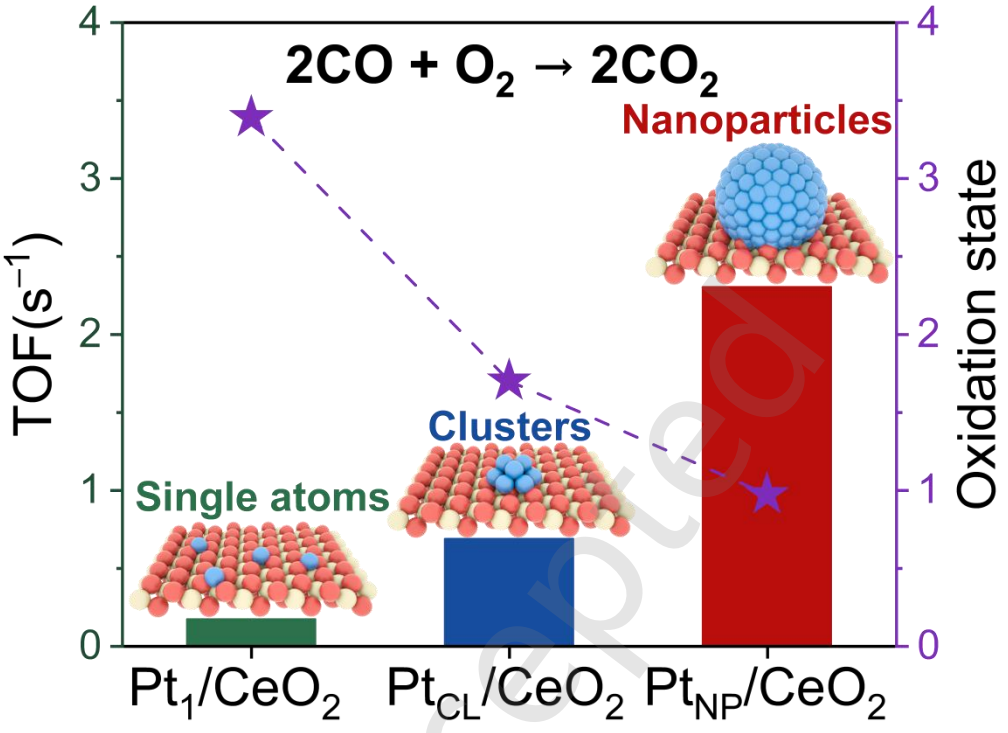


Figure. TOF of catalysts with different Pt oxidation states in the CO oxidation reaction.

This study reveals that the metallic state of Pt, rather than its dispersion alone, dictates the catalytic activity for CO oxidation on $Pt/CeO_2$ catalysts, with metallic Pt nanoparticles exhibiting the highest turnover frequency via a Mars-van Krevelen pathway. In contrast, isolated $Pt^{2+}$ atoms show weak CO binding and significantly lower activity, highlighting that preserving the metallic character is key for designing high- performance $Pt/CeO_2$ catalysts.

Nano Research

Open Access

Research Article

# Metallic states of $Pt/CeO_2$ catalysts dictate the activity for CO oxidation

Sunpei Hu[1,§], Haofan Lei[1,§], Fenglin Peng[1,§], Zizhen Xiao[1], Wenlong Wu[2], Han Yan[1,✉], Chao Ma[3,✉], and Jie Zeng[1,2,4,✉]

[1] *Hefei National Research Center for Physical Sciences at the Microscale, Key Laboratory of Strongly-Coupled Quantum Matter Physics of Chinese Academy of Sciences, Key Laboratory of Surface and Interface Chemistry and Energy Catalysis of Anhui Higher Education Institutes, Department of Chemical Physics, University of Science and Technology of China, Hefei 230026, China*
[2] *School of Chemistry & Chemical Engineering, Anhui University of Technology, Ma'anshan 243002, China*
[3] *College of Materials Science and Engineering, Hunan University, Changsha 410082, China*
[4] *Deep Space Exploration Laboratory, Hefei 230088, China*
[§] *Sunpei Hu, Haofan Lei, and Fenglin Peng contributed equally to this work.*

**Received:** 18 May 2026; **Revised:** 25 May 2026; **Accepted:** 27 May 2026

✉Address correspondence to Han Yan, hanyanustc@ustc.edu.cn; Chao Ma, cma@hnu.edu.cn; Jie Zeng, zengj@ustc.edu.cn

**Cite this article:** *Nano Research*, 2026, 19, 94908891 https://doi.org/10.26599/NR.2026.94908891

**ABSTRACT:** $Pt/CeO_2$ is a typical catalyst for CO oxidation, whose understanding of the structure-performance relationship and the factors dictating the activity remains to be fully elucidated. In this work, three $Pt/CeO_2$ catalysts with distinct Pt architectures, namely single atoms (denoted as $Pt_1$), nanoclusters (~1.0 nm, denoted as $Pt_{CL}$), and nanoparticles (~3.5 nm, denoted as $Pt_{NP}$), were investigated using aberration-corrected scanning transmission electron microscopy (STEM), X-ray photoelectron spectroscopy (XPS), X-ray absorption fine structure (XAFS), CO pulse chemisorption, and *in situ* diffuse reflectance infrared Fourier transform spectroscopy (*in situ*-DRIFTS). The results show that Pt nanoparticles exhibit the lowest oxidation state, strongest CO adsorption, and highest turnover frequency (TOF), substantially outperforming Pt clusters and single atoms. According to kinetic analysis, metallic Pt favors a Mars-van Krevelen pathway featuring efficient CO activation and carbonate-mediated turnover. In contrast, isolated $Pt^{2+}$ atoms show weak CO binding and a distinct but less active regime. It is revealed that the metallic state of Pt, rather than dispersion alone, dictates the catalytic activity for CO oxidation on $Pt/CeO_2$, which offers guidance for designing the next generation of high-performance $Pt/CeO_2$ catalysts.

**KEYWORDS:** $Pt/CeO_2$ catalyst, CO oxidation, metallic state, size effect, catalytic activity



## Introduction

As one of the most famous rare earth oxides, $CeO_2$ is known for its facile $Ce^{3+}/Ce^{4+}$ redox couple and abundance of oxygen vacancies [1–4]. These properties enable $CeO_2$ to conduct efficient activation of O-containing molecules. Moreover, the unique metal-$CeO_2$ interaction facilitates high dispersion of metal sites on $CeO_2$ support [5,6]. Therefore, supported metal/$CeO_2$ catalysts have exhibited outstanding catalytic activity in numerous reactions [7–19]. Among them, $Pt/CeO_2$ catalysts for CO oxidation have been extensively studied [20–25]. Recent advances in catalytic and functional materials highlight the importance of electronic structure, metal-support interaction, and structure-activity relationship in materials design [26–30]. The structural modulation, improvement of catalytic performance, and cognition of the structure-performance relationship are crucial, considering the significance of $Pt/CeO_2$ catalysts in both fundamental research and application in automobile exhaust purification.

The size of the Pt sites plays a key role in determining the catalytic activity of $Pt/CeO_2$ catalysts [31–34]. On the one hand, the metal utilization dramatically increases when Pt nanoparticles transform into single atoms. On the other hand, the following dominant Pt–O coordination weakens the metallic state of Pt sites. Previous studies of $CeO_2$-supported noble metal sites with varied dispersion have shown that small-sized metal nanoparticles exhibit the best activity for CO oxidation [35–38]. However, the core factor of the size effect that influences the catalytic activity for CO oxidation on $Pt/CeO_2$ catalysts remains ambiguous. Future design of highly active $Pt/CeO_2$ catalysts for CO oxidation requires clear directional guidance.

Herein, we report that the metallic state of Pt sites plays a key role in determining the catalytic activity for CO oxidation. Pt single atoms, pre-synthesized clusters (1.0 nm), and nanoparticles (3.5 nm) were supported on $CeO_2$, respectively. The structure of the Pt sites was characterized using a combination of aberration-corrected scanning transmission electron microscopy (STEM), X-ray photoelectron spectroscopy (XPS), and X-ray fine structure (XAFS). Pt nanoparticles on $CeO_2$ exhibit the lowest oxidation state and the correspondingly highest catalytic activity for CO oxidation. The metallic state of Pt sites is

crucial for CO activation, evidenced by the tested reaction orders and diffuse reflectance infrared Fourier transform spectroscopy (DRIFTS). Strategies to balance the Pt dispersion and metallic state are very likely to benefit the development of the next-generation $Pt/CeO_2$ catalysts for CO oxidation.

## Results and discussion

$CeO_2$ supports were synthesized using a simple precipitation method following a reported procedure [39]. $Ce(NO_3)_3{\cdot}6H_2O$ and ammonia solution were mixed and stirred. The precipitates were collected, dried, and calcined. As shown in Fig. S1, the transmission electron microscope (TEM) images reveal that the $CeO_2$ supports consist of nanoparticles with sizes ranging from 4.5 to 10.9 nm, exhibiting a uniform and well-dispersed morphology. We determined the specific surface area of the $CeO_2$ support from nitrogen sorption isotherms (Fig. S2a). The value obtained using the Brunauer-Emmett-Teller (BET) method is 91.4 $m^2\ g^{-1}$. Meanwhile, the X-ray diffraction (XRD) pattern (Fig. S2b) shows characteristic diffraction peaks that match the typical fluorite phase of $CeO_2$ (JCPDS No. 34-0394). This confirms the successful formation of a crystallized $CeO_2$ support. No additional impurity peaks are observed, indicating the high phase purity of the synthesized material.

To obtain $Pt/CeO_2$ catalysts with distinct Pt architectures and varied metallic states, Pt species with different sizes were loaded onto the $CeO_2$ support using distinct synthetic routes. $Pt_{NP}/CeO_2$ was synthesized via the colloidal deposition method using pre-synthesized Pt nanoparticles as the Pt source. These Pt nanoparticles (~3.5 nm, Fig. S3) were prepared via an ethylene glycol reduction method [9,40,41] and then impregnated onto $CeO_2$ support, followed by rotary evaporation at 60 °C, calcination at 400 °C for 4 h, and reduction in 10% $H_2$/Ar at 300 °C for 1 h. $Pt_{CL}/CeO_2$ was prepared similarly, except that pre-synthesized Pt nanoclusters (~1.0 nm, Fig. S4) prepared via a NaOH-assisted ethylene glycol reduction method were used instead [42]. In contrast, $Pt_1/CeO_2$ was synthesized by a conventional wet impregnation method using $H_2PtCl_6{\cdot}6H_2O$ as the precursor, followed by rotary evaporation and air calcination at 400 °C for 4 h, without a subsequent reduction step. Inductively coupled plasma-atomic emission spectrometry (ICP-AES) suggested the Pt loading constant at 0.6 wt.% for all three $Pt/CeO_2$ catalysts.

XRD patterns of the three catalysts exhibit only diffraction peaks attributed to the fluorite phase of $CeO_2$, with no detectable Pt-related reflections. This is due to the low Pt loading and the small size of the Pt species (Fig. S5). N2 adsorption isotherms show that the specific surface areas remain comparable among the three catalysts (97.1 $m^2\ g^{-1}$ for $Pt_{NP}/CeO_2$, 82.7 $m^2\ g^{-1}$ for $Pt_{CL}/CeO_2$, and 77.5 $m^2\ g^{-1}$ for $Pt_1/CeO_2$, Fig. S6). According to Raman spectroscopy (Fig. S7), all three catalysts exhibit the typical F2g vibration of fluorite $CeO_2$ at 465 $cm^{-1}$. In addition, the $Pt_1/CeO_2$ catalyst shows a vibration at 690 $cm^{-1}$ that is characteristic of the Pt–O–Ce structure [43].

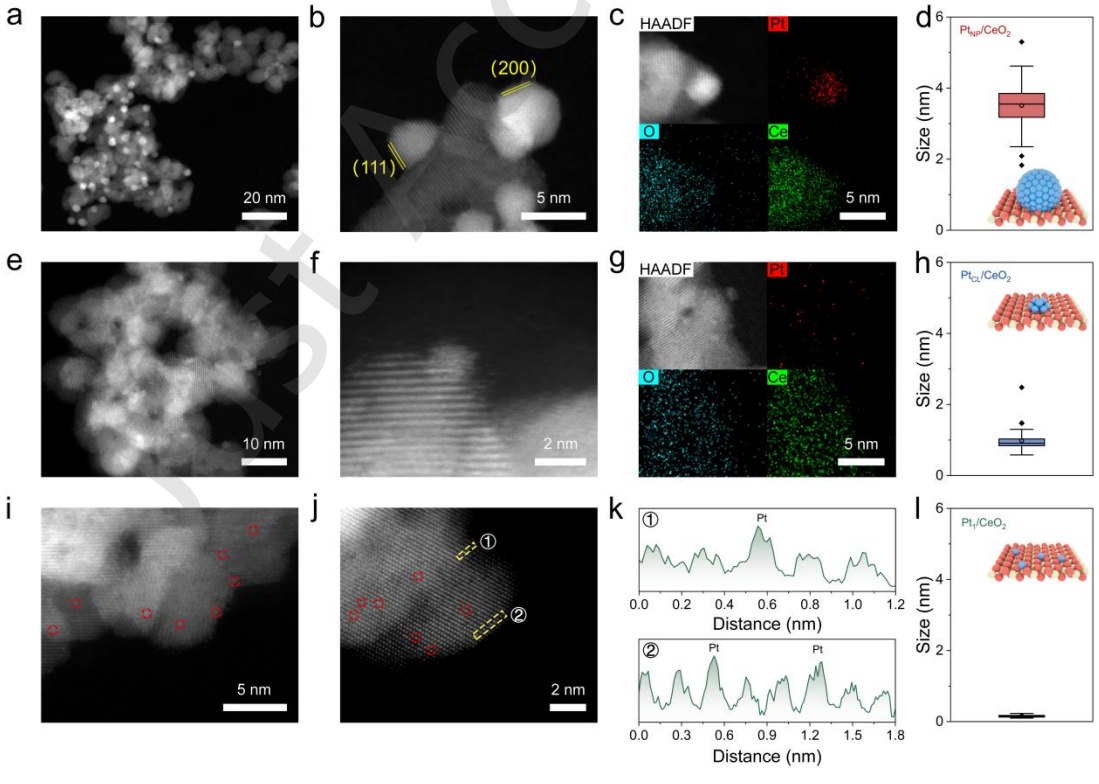


**Figure 1** **(a)** AC-HAADF-STEM image of $Pt_{NP}/CeO_2$ with low magnification. **(b)** AC-HAADF-STEM image of $Pt_{NP}/CeO_2$ with high magnification. **(c)** Elemental mapping results of $Pt_{NP}/CeO_2$. **(d)** Size distribution of Pt species and schematic diagrams of the $Pt_{NP}/CeO_2$ catalyst structure. **(e)** AC-HAADF-STEM image of $Pt_{CL}/CeO_2$ with low magnification. **(f)** AC-HAADF-STEM image of $Pt_{CL}/CeO_2$ with high magnification. **(g)** Elemental mapping results of $Pt_{CL}/CeO_2$. **(h)** Size distribution of Pt species and schematic diagrams of the $Pt_{CL}/CeO_2$ catalyst structure. **(i)** AC-HAADF-STEM image of $Pt_1/CeO_2$ with low magnification. **(j)** AC-HAADF-STEM image of $Pt_1$/CeO2 with high magnification. **(k)** Line scan intensity profiles of Pt atoms as a function of distance. **(l)** Size distribution of Pt species and schematic diagrams of the Pt1/CeO2 catalyst structure.

We used aberration-corrected high-angle-annular-dark-field scanning transmission electron microscopy (AC-HAADF-STEM) to directly visualize the Pt species on $CeO_2$. This technique takes advantage of atomic-resolution Z-contrast imaging. For $Pt_{NP}/CeO_2$, well-dispersed Pt nanoparticles with an average size of 3.5 ± 0.4 nm were observed on the $CeO_2$ surface, as shown in Fig. 1a–d and Fig. S8. The size of these Pt nanoparticles is similar to that of the pre-synthesized ones, which measured approximately 3.5 nm (Fig. S3). Moreover, these nanoparticles exhibit well-defined polyhedral morphologies with distinct facets and clear lattice fringes (Fig. 1b). Energy-dispersive X-ray spectroscopy (EDS) elemental mapping confirmed the colocalization of Pt nanoparticles with the $CeO_2$ support (Fig. 1c). For $Pt_{CL}/CeO_2$, smaller Pt clusters with an average size of 1.0 ± 0.3 nm were uniformly distributed on the $CeO_2$ surface (Fig. 1e–h and Fig. S9), which is also similar to that of the original Pt nanoclusters (~1.0 nm, Fig. S4). These clusters show irregular or elongated shapes without clear facets. EDS elemental mapping also demonstrated the presence of Pt clusters (Fig. 1g). For $Pt_1/CeO_2$, the STEM images show no Pt aggregates. Instead, isolated Pt atoms were clearly resolved as individual bright spots on the $CeO_2$ surface (Fig. 1i–l and Fig. S10). EDS elemental mapping further confirmed the presence of Pt single atoms (Fig. S11). The intensity of the bright spots was quantified by line-scan analysis of intensity profiles across selected atomic columns. As shown in Fig. 1k, due to the different atomic masses, the intensities of isolated Pt sites (Z = 78) were higher than those of the surrounding Ce adatoms (Z = 58). The single-location emergence of sites with higher intensity further demonstrated the presence of isolated Pt atoms.

The Pt 4*f* XPS spectra (Fig. 2a) reveal distinct oxidation states for the three $Pt/CeO_2$ catalysts. For $Pt_{NP}/CeO_2$, two groups of doublet peaks are observed. The peaks located at 71.2 and 74.5 eV come from metallic $Pt^0$, whereas the peaks at 72.6 and 75.9 eV come from $Pt^{2+}$. Based on calibrated peak area estimation, the ratio of $Pt^{2+}$:$Pt^0$ is 0.78:1. Based on this ratio, weighting the two oxidation states yields an average oxidation state of 0.88. The $Pt^{2+}$ in $Pt_{NP}/CeO_2$ originates from reverse oxygen spillover, a phenomenon typical for metal/$CeO_2$ catalysts [12,44–46]. For $Pt_{CL}/CeO_2$, the proportion of $Pt^0$ decreases to 25.6%, and the average oxidation state increases to 1.49. The coexistence of $Pt^{2+}$ and $Pt^0$ is frequently observed in $CeO_2$-supported Pt clusters, which can be attributed to dynamic charge transfer at the Pt-$CeO_2$ interface, promoted by phonon-assisted metal-support interaction [43,47]. In stark contrast, $Pt_1/CeO_2$ exhibits primarily $Pt^{2+}$ and $Pt^{4+}$ signals, with almost no detectable $Pt^0$ and an average oxidation state of 2.18. The $Pt^{4+}$ species observed in $Pt_1/CeO_2$, originating from residual $Pt^{4+}$ in the $H_2PtCl_6{\cdot}6H_2O$ precursor, are catalytically inert for low-temperature CO oxidation [48]. The observed trend in Pt oxidation state that decreases from $Pt_1$ to $Pt_{CL}$ to $Pt_{NP}$ can be rationalized by considering the degree of metal-support electronic interaction. Isolated Pt atoms are anchored to the $CeO_2$ surface through multiple Pt–O bonds, resulting in a strong electron withdrawal from Pt to the support, thereby stabilizing Pt in a cationic state ($Pt^{2+}$/$Pt^{4+}$). As the Pt ensemble size increases, the fraction of interfacial Pt atoms decreases, and metallic Pt–Pt bonding becomes dominant, which screens the electron transfer from the support. Consequently, Pt nanoparticles preserve a substantial metallic character.

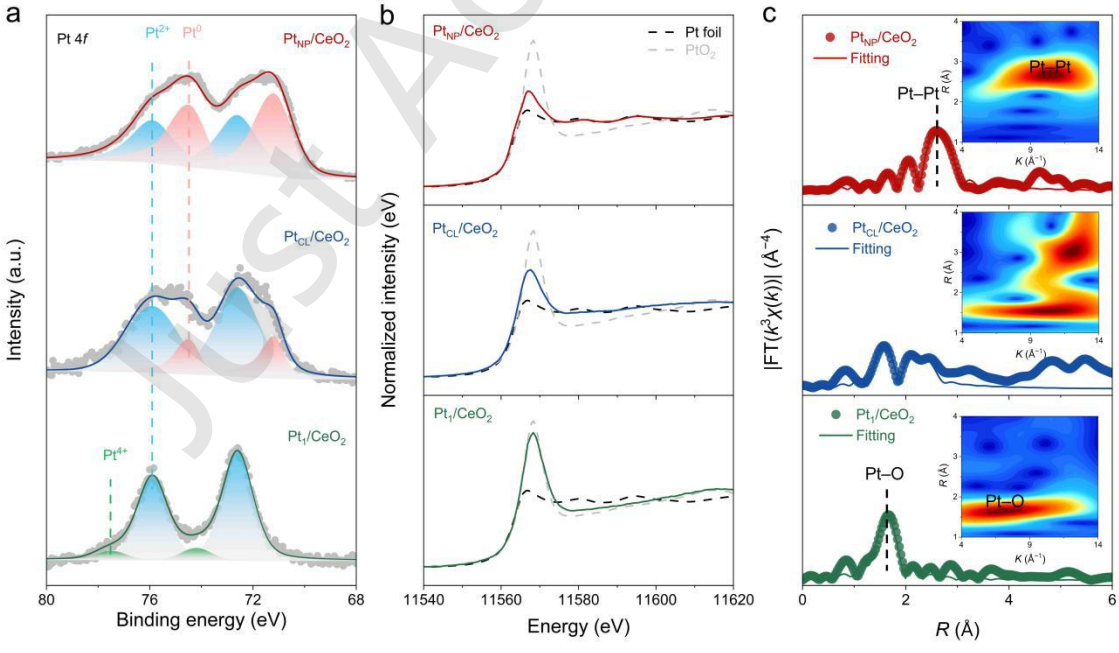


**Figure 2 (a)** Pt 4*f* XPS results of the $Pt/CeO_2$ catalysts. **(b)** XANES spectra of the $Pt/CeO_2$ catalysts at Pt $L_{III}$-edge. **(c)** Wavelet transform of the $k^3$-weighted Pt $L_{III}$-edge EXAFS of the $Pt/CeO_2$ catalysts.

The O 1*s* XPS results of the three catalysts are similar to each other (Fig. S12), ruling out the presence of unique oxygen species such as increased surface hydroxyls. Ce 3*d* XPS results (Fig. S13) show that the oxidation state of Ce is comparable across the three catalysts, being 3.72 for $Pt_{NP}/CeO_2$, 3.71 for $Pt_{CL}/CeO_2$, and 3.70 for $Pt_1/CeO_2$. This similarity suggests that the oxygen vacancy concentration on the $CeO_2$ support does not change significantly among the catalysts. Consequently, the density of oxygen vacancy and reducibility of the support are not the primary factors that

differentiate these catalysts. The real distinguishing feature is the electronic state of Pt, which is governed by the Pt ensemble size.

We performed X-ray absorption near-edge structure (XANES) and extended X-ray absorption fine structure (EXAFS) spectroscopy at the Pt $L_{III}$-edge to obtain deeper information about the local coordination environment of Pt. The XANES spectra are shown in Fig. 2b. They reveal that the white line intensity, which is related to the oxidation state, increases in the order of $Pt_{NP}/CeO_2$ < $Pt_{CL}/CeO_2$ < $Pt_1/CeO_2$. This trend agrees well with the XPS results. We then carried out wavelet transform analysis on the k3-weighted EXAFS spectra (Fig. 2c). This analysis clearly separates the Pt–O and Pt–Pt scattering contributions. For $Pt_{NP}/CeO_2$, a strong Pt–Pt contribution appears at a distance of about 2.75 Å, with a coordination number (CN) of 7.1 ± 1.1. This finding indicates the presence of metallic Pt nanoparticles. For $Pt_{CL}/CeO_2$, both Pt–O (CN = 3.3 ± 0.9 at 1.96 Å) and Pt–Pt (CN = 1.7 ± 0.8 at 2.53 Å) contributions are present, suggesting partially oxidized Pt clusters. This shortened Pt–Pt bond distance in Pt clusters indicates bond contraction, which is commonly observed in ultrasmall metal clusters due to undercoordinated surface atoms [49]. For $Pt_1/CeO_2$, only Pt–O contributions were detected, with a CN of 5.5 ± 0.7 at 1.99 Å. This confirms that the Pt species are atomically dispersed as isolated cations bonded to oxygen atoms of the $CeO_2$ support. All EXAFS fitting parameters are summarized in Table S1, and the corresponding fitting curves can be found in Fig. S14.

The catalysts were tested toward low-temperature CO oxidation. In a typical test, 60 mg of catalyst was loaded into a fixed-bed reactor, and a gas mixture of 1% CO and 4% $O_2$ balanced with Ar was fed at a total flow rate of 100 mL min1 (gas hourly space velocity = 100 L $g_{cat}^{-1}$ $h^{-1}$). The temperature was ramped from 30 to 300 °C at 2 °C $min^{-1}$. Fig. 3a shows the temperature-dependent CO conversion curves, where the temperature for 50% CO conversion is denoted as $T_{50}$. $Pt_{NP}/CeO_2$ exhibits the highest activity with a $T_{50}$ of 163 °C, which is significantly lower than that of $Pt_{CL}/CeO_2$ ($T_{50}$ = 184 °C) and $Pt_1/CeO_2$ ($T_{50}$ = 223 °C). Notably, $Pt_1/CeO_2$ shows negligible activity below 150 °C, consistent with the difficulty of activating CO on isolated $Pt^{2+}$ sites [10]. Cycling stability tests (Fig. 3b) demonstrate that $Pt_{CL}/CeO_2$ maintains stable performance over five consecutive cycles, whereas $Pt_{NP}/CeO_2$ shows slight deactivation and $Pt_1/CeO_2$ remains poorly active. For $Pt_{NP}/CeO_2$, this slight deactivation is ascribed to partial oxidation of the Pt nanoparticles under the CO oxidation reaction conditions. As shown in Fig. 3c, the apparent activation energies ($E_a$) derived from Arrhenius plots are 58.2 kJ $mol^{-1}$ for $Pt_{NP}/CeO_2$, 62.5 kJ $mol^{-1}$ for $Pt_{CL}/CeO_2$, and 86.7 kJ $mol^{-1}$ for $Pt_1/CeO_2$. The lowest $E_a$ value of $Pt_{NP}/CeO_2$ indicates its most favorable kinetics for CO oxidation.

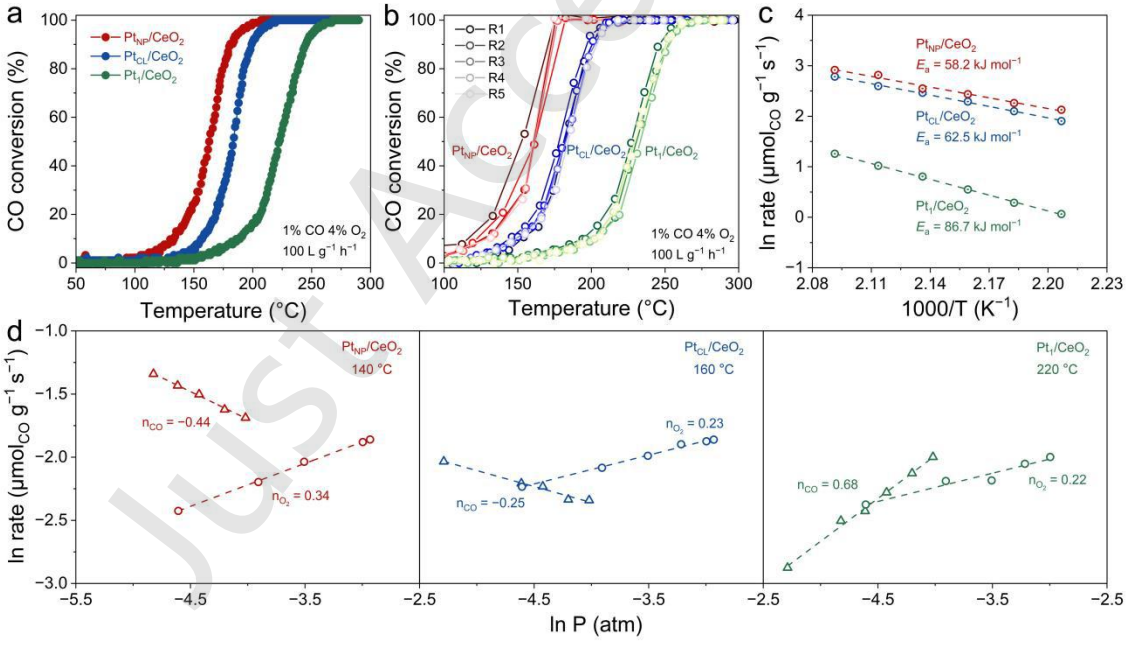


**Figure 3 (a)** Temperature-dependent CO oxidation activities of the $Pt/CeO_2$ catalysts. **(b)** Cycling stability tests of the $Pt/CeO_2$ catalysts. **(c)** Arrhenius plots of the Pt/CeO2 catalysts. **(d)** Effect of CO or $O_2$ pressure on the reaction rate of the Pt/CeO2 catalysts for CO oxidation. The pressure of CO was set from 0.5 to 2 kPa, and O2 from 1 to 6 kPa. The total pressure was 0.1 MPa.

To gain deeper insight into the reaction mechanism and the role of Pt metallic states in CO oxidation, we determined the reaction orders of CO and $O_2$ for the three $Pt/CeO_2$ catalysts within the kinetically controlled regime, as shown in Fig. 3d. For $Pt_{NP}/CeO_2$, the CO reaction order ($n_{CO}$) was 0.44, indicating strong CO adsorption on metallic Pt surfaces. The $O_2$ reaction order ($n_{O_2}$) was 0.34, suggesting that $O_2$ activation plays a significant kinetic role, consistent with the Mars-van Krevelen (MvK) mechanism in which lattice oxygen from ceria participates in CO oxidation and gas-phase $O_2$ replenishes oxygen vacancies [22,50,51]. As the Pt size decreases, the CO poisoning effect is alleviated. $Pt_{CL}/CeO_2$ exhibited a less negative $n_{CO}$ of 0.25 and a lower $n_{O_2}$ of 0.23, reflecting a mixed regime with partial retention of metallic character but increased contribution from Pt–O interfacial sites. Remarkably, $Pt_1/CeO_2$ exhibited a positive CO reaction order of +0.68, indicating weak CO adsorption on isolated $Pt^{2+}$ sites, where the surface is predominantly

CO-deficient under reaction conditions. In parallel, its $O_2$ reaction order drops to 0.22. Together, this positive CO order and lowered $O_2$ order signify that the rate-limiting step shifts from $O_2$ activation to CO activation, in stark contrast to the behavior on metallic Pt nanoparticles.

These kinetic fingerprints collectively demonstrate that the metallic state of Pt not only governs CO adsorption strength but also dictates the rate-determining steps. Metallic Pt nanoparticles enable strong CO adsorption and efficient $O_2$ activation via the MvK pathway. On the other hand, isolated Pt atoms suffer from weak CO binding, severely limiting the formation of reactive CO* intermediates and shifting the rate limitation to CO activation rather than $O_2$ dissociation. This correlation directly aligns with the metallic fraction of Pt derived from XPS and XANES (Fig. 2), reinforcing that a metallic Pt state is essential for facilitating the efficient MvK pathway for CO oxidation.

The metallic fraction of Pt was further quantified by linear combination fitting of the XANES spectra (Fig. 4a), which progressively decreases from $Pt_{NP}/CeO_2$ to $Pt_1/CeO_2$. The derived average oxidation states are 0.97, 1.70, and 3.39 for $Pt_{NP}/CeO_2$, $Pt_{CL}/CeO_2$, and $Pt_1/CeO_2$, respectively, following the same trend as the XPS results (Fig. 2a). Notably, the oxidation states obtained from linear combination fitting of the XANES spectra are systematically higher than those from XPS. This discrepancy arises from the different measurement conditions. XPS measurements must be conducted under high vacuum to ensure accurate electron signal detection and prevent surface contamination. However, under such ultrahigh vacuum conditions and prolonged X-ray or ion beam exposure, surface Pt species may undergo partial reduction, leading to an artificially lower oxidation state [52]. In contrast, XANES spectra were collected under ambient air, preserving the original oxidation state of Pt in the as-prepared catalysts. This difference has been observed, and the above explanation has been validated in our previous work [48].

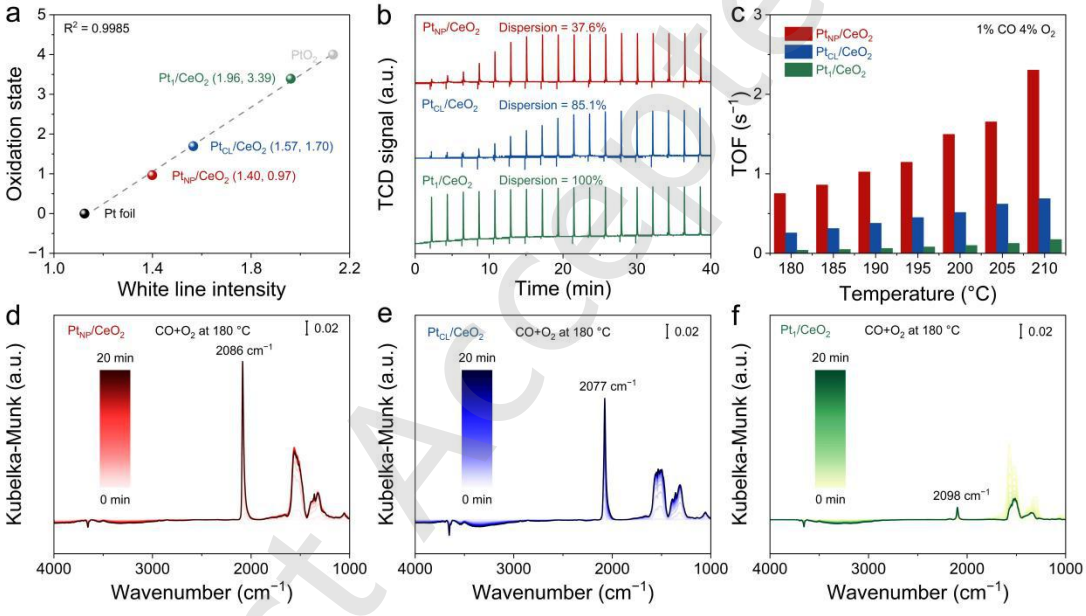


**Figure 4 (a)** Linear combination fitting of Pt $L_{III}$-edge XANES. **(b)** CO pulse and the corresponding Pt dispersion of the $Pt/CeO_2$ catalysts. **(c)** Turnover frequency (TOF) of the $Pt/CeO_2$ catalysts. **(d)** Adsorption mode of in situ-DRIFTS for $Pt_{NP}/CeO_2$. **(e)** Adsorption mode of in situ-DRIFTS for $Pt_{CL}/CeO_2$. **(f)** Adsorption mode of in situ-DRIFTS for $Pt_1/CeO_2$.

CO pulse chemisorption was then conducted to determine the dispersion and number of accessible Pt sites. The potential impact of $CeO_2$ on absorbing CO was excluded by following the reported protocol [53]. As shown in Fig. 4b, the CO uptake and the corresponding Pt dispersion increase in the order: $Pt_{NP}/CeO_2$ (37.6%) < $Pt_{CL}/CeO_2$ (85.1%) < $Pt_1/CeO_2$ (100%). It should be noted that for $Pt_1/CeO_2$, CO pulse chemisorption cannot accurately measure the dispersion because of negligible CO uptake. The nominal 100% dispersion is therefore based on the assumption, supported by AC-STEM observations (Fig. 1i), that all Pt atoms are atomically dispersed without any aggregates. However, when the turnover frequency (TOF) is calculated based on the number of surface Pt atoms (Fig. 4c), $Pt_{NP}/CeO_2$ exhibits the highest TOF (2.3 $s^{-1}$ at 210 °C), approximately three times that of $Pt_{CL}/CeO_2$ (0.7 $s^{-1}$ at 210 °C) and more than an order of magnitude higher than that of $Pt_1/CeO_2$ (0.17 $s^{-1}$ at 210 °C). These results clearly demonstrate that the intrinsic activity per surface Pt site is maximized for nanoparticles, rather than for nanoclusters or single atoms. The stark contrast in TOF points to fundamental differences in the electronic states of Pt species. For Pt single atoms, the predominant $Pt^{2+}$ and $Pt^{4+}$ species arise from direct bonding with surface oxygen atoms of $CeO_2$, which stabilizes the Pt in an oxidized state. This strong electronic perturbation, while beneficial for anchoring isolated atoms, severely suppresses the chemisorption of CO. In contrast, Pt nanoparticles retain a metallic state with only a partially oxidized interface, preserving the electronic structure necessary for efficient CO activation.

To directly verify the adsorption behavior and reaction pathway of CO oxidation over these $Pt/CeO_2$ catalysts, *in situ* diffuse reflectance infrared Fourier transform spectroscopy (DRIFTS) was performed at 180 °C under a flow of 1%

CO/4% $O_2$ (Fig. 4d–f and Fig. S15), followed by a He purge to monitor desorption (Fig. S16). Distinct differences in CO adsorption strength were observed among the three catalysts. For $Pt_{NP}/CeO_2$ (Fig. 4d and Fig. S15a), intense IR bands appeared at ~2086 $cm^{-1}$, characteristic of linearly adsorbed CO on metallic $Pt^0$ sites [54]. For $Pt_{CL}/CeO_2$ (Fig. 4e, Fig. S15b), the CO adsorption bands at ~2077 $cm^{-1}$ were notably weaker, indicating a reduced capacity for CO adsorption on Pt clusters [55]. Under our experimental conditions, neither $Pt_{NP}/CeO_2$ nor $Pt_{CL}/CeO_2$ showed clear bridge-bonded CO bands below 1900 $cm^{-1}$. This absence is probably because strong linear CO adsorption under high CO coverage overwhelms and suppresses the bridge-bonded signals [54,55]. It is noteworthy that the CO adsorption on cationic Pt single-atomic sites also appears at ~2098 $cm^{-1}$ [10]. As shown in Fig. 4f and Fig. S15c, $Pt_1/CeO_2$ shows very weak CO adsorption, due to its higher oxidation state. This discovery explains why $Pt_1/CeO_2$ did not display high catalytic activity (Fig. 3a).

Specifically, two characteristic peaks located at ~1332 and ~1566 $cm^{-1}$ were observed for all three catalysts (Fig. 4d–f, Fig. S16), which are assigned to carbonate-type species formed on the $CeO_2$ support [56,57]. The presence of these carbonate bands indicates that CO oxidation on $Pt/CeO_2$ proceeds via a carbonate-mediated pathway, wherein CO reacts with oxygen species (e.g., lattice oxygen) on ceria to generate carbonate intermediates. This pathway is consistent with the MvK mechanism inferred from the reaction order analysis. The intensity of the carbonate peaks varied drastically among the three catalysts. $Pt_{NP}/CeO_2$ exhibited the strongest carbonate signals, followed by $Pt_{CL}/CeO_2$, while $Pt_1/CeO_2$ showed only very weak carbonate peaks (Fig. 4d–f and Fig. S16). This trend correlates perfectly with the catalytic activity (Fig. 3a) and TOF (Fig. 4c). During the subsequent He purge (desorption mode, Fig. S16), the carbonate bands on $Pt_{NP}/CeO_2$ and $Pt_{CL}/CeO_2$ persisted for an extended period, indicating relatively stable carbonate intermediates. In contrast, the carbonate signals on $Pt_1/CeO_2$ decayed rapidly, further confirming that isolated Pt atoms cannot efficiently generate or stabilize carbonate species.

The strong carbonate signals observed on $Pt_{NP}/CeO_2$ are intimately linked to the metallic $Pt^0$ state. Metallic Pt provides abundant sites for CO adsorption and activation, generating a high local concentration of CO* at the Pt-$CeO_2$ interface [58]. These activated CO species readily react with surface oxygen or oxygen vacancies of $CeO_2$ to form carbonate intermediates. In contrast, isolated $Pt^{2+}$ ions on $Pt_1/CeO_2$ are incapable of stabilizing CO*, thereby starving the carbonate formation pathway. Consequently, the metallic state of Pt is the key enabler for efficient carbonate-mediated CO oxidation on $Pt/CeO_2$.

Our results highlight a critical trade-off in $Pt/CeO_2$ catalyst optimization. While single atoms maximize Pt dispersion and atom economy, they suffer from an overly oxidized state that suppresses CO activation and carbonate turnover. Conversely, large Pt nanoparticles exhibit superior intrinsic activity but lower Pt utilization. Therefore, an optimal catalyst architecture for CO oxidation should balance metallic character and dispersion. Our work establishes the metallic state of Pt as a key descriptor for CO oxidation on $Pt/CeO_2$, providing a clear rationale for moving beyond the simplistic pursuit of full dispersion. The following efforts may focus on precisely tuning the Pt oxidation state via controlled reduction protocols or support facet engineering to achieve the optimum compromise between Pt utilization and intrinsic activity. For instance, the development of strategies toward lowering the oxidation state of Pt single atoms while maintaining the dispersion is very likely to achieve the breakthrough in the future.

## Conclusion

In summary, we systematically investigated $Pt/CeO_2$ catalysts featuring three distinct Pt architectures, namely Pt single atoms ($Pt_1$), nanoclusters ($Pt_{CL}$, ~1.0 nm), and nanoparticles ($Pt_{NP}$, ~3.5 nm), for CO oxidation. Using multiple techniques such as AC-HAADF-STEM, XPS, XAFS, CO chemisorption, and *in situ*-DRIFTS, we found that the metallic state of Pt, not simply its dispersion, determines the catalytic activity. Pt nanoparticles exhibit the lowest oxidation state, the strongest CO uptake, and the highest intrinsic activity, thus greatly outperforming Pt clusters and Pt single atoms. Kinetic analysis shows that metallic Pt favors a MvK pathway with efficient CO activation and carbonate-mediated turnover. In contrast, isolated $Pt^{2+}$ sites bind CO only weakly and operate in a distinct but less active regime. Therefore, we establish the metallic state as a crucial descriptor for CO oxidation on $Pt/CeO_2$, providing clear guidance for future catalyst design. Optimizing the metallic character of Pt is essential to achieve high-performance $Pt/CeO_2$ catalysts for low-temperature CO oxidation and related reactions.

**Electronic Supplementary Material:** Supplementary material (Figures S1–S16, and Table S1) is available in the online version of this article at https://doi.org/10.26599/NR.2026.94908891.

## Data availability

All data needed to support the conclusions in the paper are presented in the manuscript and the Electronic Supplementary Material. Additional data related to this paper may be requested from the corresponding author upon request.

## Acknowledgements

This work was supported by National Key Research and Development Program of China (2021YFA1500500), NSFC (22525021, 22302185, 22221003, 22250007, 22361162655), the Science and Technology Development Fund (FDCT) of Macao S.A.R (0070/2023/AFJ), Fundamental Research Funds for the Central Universities (WK9990000167), Special Science and Technology Innovation Program for Carbon Peak and Carbon Neutralization of Jiangsu Province (Grant No. BE2025014), the State Key Laboratory of Catalysis (2024SKL-A-011), University of Science and Technology of China-Xinjiang Normal University Counterpart Cooperation and Development Joint Fund, the Key Project of Natural Science Foundation of Anhui Province (2508085ZD020), International Partnership Program of Chinese Academy of Sciences (123GJHZ2022101GC). H.Y. acknowledges support from the USTC Tang Scholar. J.Z. acknowledges support from the New Cornerstone Science Foundation through the XPLORER PRIZE. This work was partially carried out at the

Instruments Center for Physical Science, University of Science and Technology of China. We thank the 1W1B-XAFS Beamline of Beijing Synchrotron Radiation Facility (https://cstr.cn/31109.02.BSRF.1W1B) for providing technical support and assistance in XAFS data collection.

## Declaration of competing interest

All the contributing authors report no conflict of interests in this work.

## Author contribution statement

S. H.: Data curation, project administration, validation, writing manuscript, experimental design. H. L.: Data curation, experimental design. F. P.: Data curation, experimental design. Z. X.: experimental design. W. W.: Writing-review & editing. H. Y.: Conceptualization, Supervision, Writing-review & editing. C. M.: Conceptualization, Supervision, Writing-review & editing. J. Z.: Conceptualization, Funding acquisition, Supervision, Writing -review & editing. All the authors have approved the final manuscript."

## Use of AI statement

None.

## References

[1] Esch, F.; Fabris, S.; Zhou, L.; Montini, T.; Africh, C.; Fornasiero, P.; Comelli, G.; Rosei, R. Electron Localization Determines Defect Formation on Ceria Substrates. *Science* **2005**, 309, 752–755.

[2] Liu, X.; Zhou, K.; Wang, L.; Wang, B.; Li, Y. Oxygen Vacancy Clusters Promoting Reducibility and Activity of Ceria Nanorods. *J. Am. Chem. Soc.* **2009**, 131, 3140–3141.

[3] Pang, D.; Li, W.; Zhang, N.; He, H.; Mao, S.; Chen, Y.; Cao, L.; Li, C.; Li, A.; Han, X. Direct observation of oxygen vacancy formation and migration over ceria surface by *in situ* environmental transmission electron microscopy. *J. Rare Earths* **2024**, 42, 676–682.

[4] Lin, F.; Hoang, D. T.; Tsung, C.-K.; Huang, W.; Lo, S. H.-Y.; Wood, J. B.; Wang, H.; Tang, J.; Yang, P. Catalytic properties of Pt cluster-decorated CeO2 nanostructures. *Nano Res.* **2011**, 4, 61–71.

[5] Cargnello, M.; Doan-Nguyen, V. V. T.; Gordon, T. R.; Diaz, R. E.; Stach, E. A.; Gorte, R. J.; Fornasiero, P.; Murray, C. B. Control of Metal Nanocrystal Size Reveals Metal-Support Interface Role for Ceria Catalysts. *Science* **2013**, 341, 771–773.

[6] Lin, F.; Hoang, D. T.; Tsung, C. K.; Huang, W.; Lo, S. H. Y.; Wood, J. B.; Wang, H.; Tang, J.; Yang, P. Insight of the stability and activity of platinum single atoms on ceria. *Nano Res.* **2019**, 12, 1401–1409.

[7] Fu, X.-P.; Wu, C.-P.; Wang, W.-W.; Jin, Z.; Liu, J.-C.; Ma, C.; Jia, C.-J. Boosting reactivity of water-gas shift reaction by synergistic function over $CeO_{2-x}$/$CoO_{1-x}$/Co dual interfacial structures. *Nat. Commun.* **2023**, 14, 6851.

[8] Liu, H.-X.; Li, S.-Q.; Wang, W.-W.; Yu, W.-Z.; Zhang, W.-J.; Ma, C.; Jia, C.-J. Partially sintered copper–ceria as excellent catalyst for the high-temperature reverse water gas shift reaction. *Nat. Commun.* **2022**, 13, 867.

[9] Hu, X.-C.; Fu, X.-P.; Wang, W.-W.; Wang, X.; Wu, K.; Si, R.; Ma, C.; Jia, C.-J.; Yan, C.-H. Ceria-supported ruthenium clusters transforming from isolated single atoms for hydrogen production via decomposition of ammonia. *Appl. Catal. B* **2020**, 268, 118726.

[10] Yan, H.; Lei, H.; Qin, X.; Liu, J.-C.; Cai, L.; Hu, S.; Xiao, Z.; Peng, F.; Wang, W.-W.; Jin, Z.; Yi, X.; Zheng, A.; Ma, C.; Jia, C.-J.; Zeng, J. Facet-Dependent Diversity of Pt–O Coordination for $Pt_1/CeO_2$ Catalysts Achieved by Oriented Atomic Deposition. *Angew. Chem. Int. Ed.* **2024**, 63, e202411264.

[11] Hu, S.; Lei, H.; Shi, J.; Ye, Y.; Peng, F.; Wu, W.; Zhang, J.; Yan, H.; Ma, C.; Zeng, J. $CeO_2$-supported bi-layer Pt clusters for anti-Markovnikov alkene hydrosilylation. *Sci. China Chem.* **2025**, 69, 946–952.

[12] Zhang, Y.; Zhang, N.; Liu, Y.; Lei, H.; Zhou, T.; Wu, W.; Wang, W.-W.; Yan, H.; Ma, C.; Shimizu, K.; Jia, C.-J.; Zeng, J. Reversible aggregation-redispersion of Cu sites in $Cu/CeO_2$ catalysts with unlocked hydrogenation activity. *Sci. Adv.* **2026**, 12, eaed2774.

[13] Zhou, X.; Ren, J.; Xu, W.; Wang, Y.; Sun, Y.; Li, W.; Zhang, S.; Qu, Y. Cluster Density-Dependent Electronic Metal-Support Interactions in $Rh/CeO_2$ for Enhanced Styrene Hydroformylation. *J. Phys. Chem. Lett.* **2025**, 16, 8707–8713.

[14] Herrero, J.; He, P.; Yang, F.; Weng, J.; LiBretto, N. J.; Mainardi, D. S.; Miller, J. T.; Wu, Y.; Xiao, Y. Synergy of Cu(I) and oxygen vacancies in $CO_2$ hydrogenative coupling to ethanol on $Cu/CeO_{2-x}$ catalysts. *Nano Res.* **2025**, 18, 94907518.

[15] Xu, Q.; Cheng, X.; Zhang, N.; Tu, Y.; Wu, L.; Pan, H.; Hu, J.; Ding, H.; Zhu, J.; Li, Y. Unraveling the advantages of $Pd/CeO_2$ single-atom catalysts in the NO + CO reaction by model catalysts. *Nano Res.* **2023**, 16, 8882–8892.

[16] Xie, S.; Xi, Y.; Xie, J.; Wei, J.; Liu, Q.; Yang, Y.; Lin, H.; Bai, Y.; Wang, T.; Su, P.; Li, Z.; Tang, Y. A highly dispersed $Pd/CeO_2$ catalyst for boosting C–O bond cleavage of diphenyl ether. *J. Rare Earths* **2025**, 43, 962–970.

[17] Xin, P.; Li, J.; Xiong, Y.; Wu, X.; Dong, J.; Chen, W.; Wang, Y.; Gu, L.; Luo, J.; Rong, H.; Chen, C.; Peng, Q.; Wang, D.; Li, Y. Revealing the Active Species for Aerobic Alcohol Oxidation by Using Uniform Supported Palladium Catalysts. *Angew. Chem. Int. Ed.* **2018**, 57, 4642–4646.

[18] Li, Z.; Zhang, M.; Zhang, L.; Dong, X.; Leng, L.; Horton, J. H.; Wang, J. Engineering the atomic interface of porous ceria nanorod with single palladium atoms for hydrodehalogenation reaction. *Nano Res.* **2021**, 15, 1338–1346.

[19] Zhang, J.; Wang, Z.; Chen, W.; Xiong, Y.; Cheong, W.-C.; Zheng, L.; Yan, W.; Gu, L.; Chen, C.; Peng, Q.; Hu, P.; Wang, D.; Li, Y. Tuning Polarity of Cu–O Bond in Heterogeneous Cu Catalyst to Promote Additive-free Hydroboration of Alkynes. *Chem.* **2020**, 6, 725–737.

[20] Jones, J.; Xiong, H.; DeLaRiva, A. T.; Peterson, E. J.; Pham, H.; Challa, S. R.; Qi, G.; Oh, S.; Wiebenga, M. H.; Pereira Hernández, X. I.; Wang, Y.; Datye, A. K. Thermally stable single-atom platinum-on-ceria catalysts via atom trapping. *Science* **2016**, 353, 150–154.

[21] Nie, L.; Mei, D.; Xiong, H.; Peng, B.; Ren, Z.; Hernandez, X. I. P.; DeLaRiva, A.; Wang, M.; Engelhard, M. H.; Kovarik, L.; Datye, A. K.; Wang, Y. Activation of surface lattice oxygen in single-atom $Pt/CeO_2$ for low-temperature CO oxidation. *Science* **2017,** 358, 1419–1423.

[22] Wang, H.; Liu, J. X.; Allard, L. F.; Lee, S.; Liu, J.; Li, H.; Wang, J.; Wang, J.; Oh, S. H.; Li, W.; Flytzani-Stephanopoulos, M.; Shen, M.; Goldsmith, B. R.; Yang, M. Surpassing the single-atom catalytic activity limit through paired Pt–O–Pt ensemble built from isolated $Pt_1$ atoms. *Nat. Commun.* **2019**, 10, 3808.

[23] Maurer, F.; Jelic, J.; Wang, J.; Gänzler, A.; Dolcet, P.; Wöll, C.; Wang, Y.; Studt, F.; Casapu, M.; Grunwaldt, J.-D. Tracking the formation, fate and consequence for catalytic activity of Pt single sites on $CeO_2$. *Nat. Catal.* **2020**, 3, 824–833.

[24] Tan, W.; Xie, S.; Le, D.; Diao, W.; Wang, M.; Low, K. B.; Austin, D.; Hong, S.; Gao, F.; Dong, L.; Ma, L.; Ehrlich, S. N.; Rahman, T. S.; Liu, F. Fine-tuned local coordination environment of Pt single atoms on ceria controls catalytic reactivity. *Nat. Commun.* **2022**, 13, 7070.

[25] Liu, H.; Li, D.; Guo, J.; Li, Y.; Liu, A.; Bai, Y.; He, D. Recent advances on catalysts for preferential oxidation of CO. *Nano Res.* **2023**, 16, 4399–4410.

[26] Guo, Y.; Liu, Z.; Zhou, D.; Zhang, M.; Zhang, Y.; Li, R.; Liu, S.; Wang, D.; Dai, Z. Competition and synergistic effects of Ru-based single-atom and cluster catalysts in electrocatalytic reactions. *Sci. China Mater.* **2024**, 67, 1706–1720.

[27] Wang, S.; Wang, L.; Zhou, X.; Fang, J.; Deng, C.; Wang, D. Design principles of single-atom catalysts anchored over porous materials for green catalysis and conversion. *Nano Res.* **2025**, 18, 94907137.

[28] Yang, X.; Ma, L.; Wang, S.; Hu, X.; Li, B.; Li, W.; Wang, D.; Dai, Z. Electrochemiluminescence-based multiplex immunoassays for multianalyte bioanalysis: Signal encoding strategies and analytical perspectives. *Electrochem. Commun.* **2026**, 186, 108130.

[29] Pan, H.; Liu, B.; Wang, D.; Zhao, S.; Yuan, Z.; Zhuang, Z.; Yang, J.; Dou, Y.; Li, Z.; Zhang, M.; Cui, W.-G.; Guan, S.; Fan, Y.; Zhang, H. Research progress on Ti-based materials for $MgH_2$ hydrogen storage systems. Compos. *Funct. Mater.* **2025**, 1, 20250201.

[30] Yuan, H.; Chen, P.; Li, X.; Xu, X.; Qian, W.; Zhang, H.; Wang, Z.; Fu, H.; Wang, D.; He, D. Scalable fiber-skeleton-reinforced graphene-assembled films enabling wash-durable wearable heating. *Nano Res.* **2026**, 19, 94908671.

[31] Yuan, K.; Guo, Y.; Lin, Q.-L.; Huang, L.; Ren, J.-T.; Liu, H.-C.; Yan, C.-H.; Zhang, Y.-W. Size effect-tuned water gas shift reaction activity and pathway on ceria supported platinum catalysts. *J. Catal.* **2021**, 394, 121–130.

[32] Wang, C.; Mao, S.; Wang, Z.; Chen, Y.; Yuan, W.; Ou, Y.; Zhang, H.; Gong, Y.; Wang, Y.; Mei, B.; Jiang, Z.; Wang, Y. Insight into Single-Atom-Induced Unconventional Size Dependence over $CeO_2$-Supported Pt Catalysts. *Chem* **2020**, 6, 752–765.

[33] Ge, S.; Fan, W.; Tang, X.; Cui, Y.; Wang, D.; Gong, X.-Q.; Dai, S.; Lou, Y.; Tang, J.; Guo, Y.; Zhan, W.; Wang, L.; Guo, Y. Revealing the Size Effect of Ceria Nanocube-Supported Platinum Nanoparticles in Complete Propane Oxidation. *ACS Catal.* **2024**, 14, 2532–2544.

[34] Song, J.; Yang, Y.; Liu, S.; Li, L.; Yu, N.; Fan, Y.; Chen, Z.; Kuai, L.; Geng, B. Dispersion and support dictated properties and activities of Pt/metal oxide catalysts in heterogeneous CO oxidation. *Nano Res.* **2021**, 14, 4841–4847.

[35] Ligthart, D. A.; van Santen, R. A.; Hensen, E. J. Supported rhodium oxide nanoparticles as highly active CO oxidation catalysts. *Angew. Chem. Int. Ed.* **2011**, 50, 5306–5310.

[36] Chen, S.; Luo, L.; Jiang, Z.; Huang, W. Size-Dependent Reaction Pathways of Low-Temperature CO Oxidation on $Au/CeO_2$ Catalysts. *ACS Catal.* **2015**, 5, 1653–1662.

[37] Guo, L. W.; Du, P. P.; Fu, X. P.; Ma, C.; Zeng, J.; Si, R.; Huang, Y. Y.; Jia, C. J.; Zhang, Y. W.; Yan, C. H. Contributions of distinct gold species to catalytic reactivity for carbon monoxide oxidation. *Nat. Commun.* **2016**, 7, 13481.

[38] Ma, K.; Liao, W.; Shi, W.; Xu, F.; Zhou, Y.; Tang, C.; Lu, J.; Shen, W.; Zhang, Z. Ceria-supported Pd catalysts with different size regimes ranging from single atoms to nanoparticles for the oxidation of CO. *J. Catal.* **2022**, 407, 104–114.

[39] Chen, H.-I.; Chang, H.-Y. Synthesis of nanocrystalline cerium oxide particles by the precipitation method. *Ceram. Int.* **2005**, 31, 795–802.

[40] Wang, Y.; Ren, J.; Deng, K.; Gui, L.; Tang, Y. Preparation of Tractable Platinum, Rhodium, and Ruthenium Nanoclusters with Small Particle Size in Organic Media. *Chem. Mater.* **2000**, 12, 1622–1627.

[41] Yan, L.-Y.; Fu, X.-P.; Wang, W.-W.; Jia, C.-J. Atmosphere-induced Ru-Ov-$CeO_2$ interface for alleviating hydrogen inhibitory effect toward ammonia decomposition. *Appl. Catal. B* **2025**, 378.

[42] Chen, C.; Chen, F.; Zhang, L.; Pan, S.; Bian, C.; Zheng, X.; Meng, X.; Xiao, F. S. Importance of platinum particle size for complete oxidation of toluene over Pt/ZSM-5 catalysts. *Chem. Commun.* **2015**, 51, 5936–5938.

[43] Yan, H.; Qin, X.; Liu, J.-C.; Cai, L.; Xu, P.; Song, J.-J.; Ma, C.; Wang, W.-W.; Jin, Z.; Jia, C.-J. Releasing the limited catalytic activity of $CeO_2$-supported noble metal catalysts via UV-induced deep dechlorination. *J. Catal.* **2022**, 413, 703–712.

[44] Vayssilov, G. N.; Lykhach, Y.; Migani, A.; Staudt, T.; Petrova, G. P.; Tsud, N.; Skala, T.; Bruix, A.; Illas, F.; Prince, K. C.; Matolin, V.; Neyman, K. M.; Libuda, J. Support nanostructure boosts oxygen transfer to catalytically active platinum nanoparticles. *Nat. Mater.* **2011**, 10, 310–315.

[45] Wang, C.-X.; Zhang, L.-Y.; Wang, W.-W.; Yang, F.; Jia, C.-J. Unveiling Reversible Evolution of Single-Atom Catalysts Driven by Reverse Oxygen Spillover of $CeO_2$. *ACS Catal.* **2024**, 14, 9421–9430.

[46] Su, Y.-Q.; Xia, G.-J.; Qin, Y.; Ding, S.; Wang, Y.-G. Lattice oxygen self-spillover on reducible oxide supported metal cluster: the water-gas shift reaction on $Cu/CeO_2$ catalyst. *Chem. Sci.* **2021**, 12, 8260–8267.

[47] Daelman, N.; Capdevila-Cortada, M.; Lopez, N. Dynamic charge and oxidation state of $Pt/CeO_2$ single-atom catalysts. **Nat. Mater**. 2019, 18, 1215–1221.

[48] Lei, H.; Zhang, N.; Hu, S.; Peng, F.; Zhou, J.; He, J.; Zhang, L.; Wang, H.; Ma, C.; Yan, H.; Shimizu, K.; Zeng, J. Thermally Triggered Redox Flexibility of $Pt/CeO_2$ Cluster Catalyst Against *In-Situ* Atomic Redispersion. *Angew. Chem. Int. Ed.* **2025**, 64, e202509239.

[49] Lytle, F. W.; Greegor, R. B.; Marques, E. C.; Sandstrom, D. R.; Via, G. H.; Sinfelt, J. H. Structural genesis of Pt on $SiO_2$: Determination by X-ray absorption spectroscopy. *J. Catal.* **1985**, 95, 546–557.

[50] Zhang, Z.; Tian, J.; Lu, Y.; Yang, S.; Jiang, D.; Huang, W.; Li, Y.; Hong, J.; Hoffman, A. S.; Bare, S. R.; Engelhard, M. H.; Datye, A. K.; Wang, Y. Memory-dictated dynamics of single-atom Pt on $CeO_2$ for CO oxidation. *Nat. Commun.* **2023**, 14, 2664.

[51] Ke, J.; Zhu, W.; Jiang, Y.; Si, R.; Wang, Y.-J.; Li, S.-C.; Jin, C.; Liu, H.; Song, W.-G.; Yan, C.-H.; Zhang, Y.-W. Strong Local Coordination Structure Effects on Subnanometer $PtO_x$ Clusters over $CeO_2$ Nanowires Probed by Low-Temperature CO Oxidation. *ACS Catal.* **2015**, 5, 5164–5173.

[52] Vovk, E. I.; Kalinkin, A. V.; Smirnov, M. Y.; Klembovskii, I. O.; Bukhtiyarov, V. I. XPS Study of Stability and Reactivity of Oxidized Pt Nanoparticles Supported on $TiO_2$. *J. Phys. Chem. C* **2017**, 121, 17297–17304.

[53] Takeguchi, T.; Manabe, S.; Kikuchi, R.; Eguchi, K.; Kanazawa, T.; Matsumoto, S.; Ueda, W. Determination of dispersion of precious metals on $CeO_2$-containing supports. *Appl. Catal. A* **2005**, 293, 91–96.

[54] Resasco, J.; DeRita, L.; Dai, S.; Chada, J. P.; Xu, M.; Yan, X.; Finzel, J.; Hanukovich, S.; Hoffman, A. S.; Graham, G. W.; Bare, S. R.; Pan, X.; Christopher, P. Uniformity Is Key in Defining Structure-Function Relationships for Atomically Dispersed Metal Catalysts: The Case of $Pt/CeO_2$. *J. Am. Chem. Soc.* **2020**, 142, 169–184.

[55] Kale, M. J.; Christopher, P. Utilizing Quantitative *in Situ* FTIR Spectroscopy To Identify Well-Coordinated Pt Atoms as the Active Site for CO Oxidation on $Al_2O_3$-Supported Pt Catalysts. *ACS Catal.* **2016**, 6, 5599–5609.

[56] Feng, X.; Wang, Z.; Mu, L.; Chen, Z.; Liang, J.; Xiao, C. The different evolution behaviors of carbonate-like species on $Pt/CeO_2$ and $Pt/Al_2O_3$ by *in situ* DRIFTS-MS study. *Catal. Today* **2022**, 400–401, 82–88.

[57] Cheng, X.; Tu, Y.; Zhang, D.; Han, D.; Huang, L.; Hu, J.; Ding, H.; Xu, Q.; Zhu, J. CO adsorption, activation, and oxidation on $CeO_2$(111)-supported Fe model catalyst surfaces. *Nano Res.* **2025**, 18.

[58] Simanenko, A.; Kastenmeier, M.; Piliai, L.; Kosto, Y.; Skála, T.; Tsud, N.; Mehl, S.; Vorokhta, M.; Matolínová, I.; Lykhach, Y.; Libuda, J. Probing the redox capacity of Pt–$CeO_2$ model catalyst for low-temperature CO oxidation. *J. Mater. Chem. A* **2023**, 11, 16659–16670.

# Electronic Supplementary Material

# Metallic states of $Pt/CeO_2$ catalysts dictate the activity for CO oxidation

Sunpei Hu[1,§], Haofan Lei[1,§], Fenglin Peng[1,§], Zizhen Xiao[1], Wenlong Wu[2], Han Yan[1,✉], Chao Ma[3,✉], and Jie Zeng[1,2,4,✉]

[1] *Hefei National Research Center for Physical Sciences at the Microscale, Key Laboratory of Strongly-Coupled Quantum Matter Physics of Chinese Academy of Sciences, Key Laboratory of Surface and Interface Chemistry and Energy Catalysis of Anhui Higher Education Institutes, Department of Chemical Physics, University of Science and Technology of China, Hefei 230026, China*
[2] *School of Chemistry & Chemical Engineering, Anhui University of Technology, Ma'anshan 243002, China*
[3] *College of Materials Science and Engineering, Hunan University, Changsha 410082, China*
[4] *Deep Space Exploration Laboratory, Hefei 230088, China*
[§] *Sunpei Hu, Haofan Lei, and Fenglin Peng contributed equally to this work.*

✉ Address correspondence to Han Yan, hanyanustc@ustc.edu.cn; Chao Ma, cma@hnu.edu.cn; Jie Zeng, zengj@ustc.edu.cn

Supporting information to https://doi.org/10.26599/NR.2026.94908891

**This file includes:**

## S1. METHODS

### Preparation of the catalysts

**Chemicals and materials.** The precursors used in this work were Cerium(III) nitrate hexahydrate (Shanghai Chemical Reagent Co, 99%), ammonium hydroxide solution (Shanghai Chemical Reagent Co, 25%), hydrogen Chloroplatinic(IV) acid (Sigma-Aldrich, 99%), NaOH (Shanghai Chemical Reagent Co, 99%), ethylene glycol (Shanghai Chemical Reagent Co, 99%), ethanol (Shanghai Chemical Reagent Co, 99%), poly(vinylpyrrolidone) (Sigma-Aldrich, $M_n$~55,000), acetone (Shanghai Chemical Reagent Co, 99%), hexane (Shanghai Chemical Reagent Co, 99%), hydrochloric acid solution (Shanghai Chemical Reagent Co, 36%). All chemical reagents were used as received without further purification. All aqueous solutions were prepared using deionized water with a resistivity of 18.2 MΩ·cm.

**Synthesis of $CeO_2$ support.** $CeO_2$ nanoparticles were synthesized using the precipitation method. In a typical synthesis using the precipitation method, 2.0 g of $Ce(NO_3)_3{\cdot}6H_2O$ were dissolved in 100 mL of Millipore water. Then 1 mL of $NH_3$ $H_2O$ was added and stirred for 24 h. Next, the precipitation was washed several times and separated by centrifugation (10 krpm, 5 min). The collected powders were dried at 60 °C overnight and went through air calcination at 400 °C for 4 h.

**Synthesis of Pt nanoparticle ($Pt_{NP}$) suspension solution.** A solution of poly(vinylpyrrolidone) (PVP, 400 mg) in ethylene glycol (30 mL) was prepared directly in the reaction vessel and brought to 150 °C with stirring. Subsequently, 2 mL of chloroplatinic(IV) acid solution ($H_2PtCl_6{\cdot}6H_2O$, 10 $mg_{Pt}$ $mL^{-1}$) was introduced into the heated system. The color of the solution rapidly turned black. The mixture was kept stirring for 30 min at 150 °C. The reaction was then cooled rapidly by transferring the reactor vessel to an ice-water bath. The Pt nanoparticles were precipitated by adding acetone (60 mL) to give a black suspension, which was sonicated for 1 min. The precipitate was then isolated by ultracentrifugation (10 krpm, 5 min), and the yellow supernatant was decanted away to leave a black solid. This was further purified to remove excess PVP and ethylene glycol by 3–5 cycles of dissolution in ethanol (15 mL) followed by precipitation with hexane (75 mL) and isolation by centrifugation. The final products were redispersed in 10 mL ethanol and stored at room temperature.

**Preparation of $Pt_{NP}/CeO_2$.** $Pt_{NP}/CeO_2$ was prepared by using an incipient wetness impregnation method. Typically, 400 mg of $CeO_2$ support was dispersed in 40 mL of deionized water. Then, a certain volume of $Pt_{NP}$ suspension solution was added to the mixture. After stirring at room temperature for 1 h, ethanol was removed by rotary evaporation at 60 °C. Then, the powder was calcined at 400 °C for 4 h. After calcination, the powder was reduced in 10% $H_2$/Ar with a flow rate of 50 mL $min^{-1}$ at 300 °C for 1 h. The Pt loading was set as 0.6 wt.%.

**Synthesis of Pt cluster ($Pt_{CL}$) suspension solution.** Chloroplatinic(IV) acid (40.0 mg) and NaOH (220 mg) were dissolved in 20 mL ethylene glycol (EG) with an appropriate amount of deionized water in a 100 mL three-necked flask and stirred at room temperature for 1 h to completely dissolve NaOH. Then the mixed solution was rapidly heated to 90 °C with $N_2$ as protective gas for 2 h. When the color of the solution changed from yellow to dark brown without any precipitation, the Pt nanoclusters were formed. The platinum nanoclusters were extracted by adding a certain amount of 0.3 mol $L^{-1}$ HCl solution and isolated by centrifugation (10 krpm, 5 min). The final products were redispersed in 5 mL ethanol containing 400 mg of PVP and stored at room temperature.

**Preparation of $Pt_{CL}/CeO_2$.** $Pt_{CL}/CeO_2$ was prepared by using an incipient wetness impregnation method. Typically, 400 mg of $CeO_2$ support was dispersed in 40 mL of deionized water. Then, a certain volume of $Pt_{CL}$ suspension solution was added to the mixture. After stirring at room temperature for 1 h, ethanol was removed by rotary evaporation at 60 °C. Then, the powder was calcined at 400 °C for 4 h. After calcination, the powder was reduced in 10% $H_2$/Ar with a flow rate of 50 mL $min^{-1}$ at 300 °C for 1 h. The Pt loading was set as 0.6 wt.%.

**Preparation of $Pt_1/CeO_2$.** The $Pt_1/CeO_2$ catalysts were prepared via the impregnation method. Typically, a certain amount of aqueous $H_2PtCl_6{\cdot}6H_2O$ solution was mixed with $CeO_2$ support (400 mg) in 40 mL of Millipore water. After stirring for 2 h, the sample was collected in a rotary evaporator at 60 °C. The catalysts were acquired after air calcination at 400 °C for 4 h. The Pt loading was set as 0.6 wt.%.

**S2. Materials characterization**

**ICP-AES experiments.** Inductively coupled plasma-atomic emission spectrometry (ICP-AES, Atomscan Advantage, Thermo Jarrell Ash, USA) was used to determine the loadings of metal species. The samples were dissolved by using a mixture of 3mL 30% $H_2O_2$ and aqua regia (volume ratio of 2:1) solution. Then, the solution volume was diluted to 10 mL.

**Electron microscope experiments.** The transmission electron microscopy (TEM) image was taken on a HT-7700 Exalens Transmission electron microscope operating at an acceleration voltage of 100 kV. The high-angle annular dark-field scanning transmission electron microscopy (HAADF-STEM), and energy dispersive spectrometer (EDS) element mapping images were collected on a Thermo scientific Themis Z (3.2) field-emission transmission electron microscope operating at an acceleration voltage of 300 kV.

**Surface area measurements.** TriStar II Plus Builder surface area analyzer was used for the nitrogen sorption measurements at 77 K. The samples were degassed at 100 °C for 6 h under vacuum. The calculation of specific surface area was based on the Brunauer-Emmett-Teller (BET) method.

**XRD measurements.** X-ray diffraction (XRD) patterns were recorded by using a Philips X'Pert Pro Super diffractometer (Cu-$K_\alpha$ radiation, λ = 1.54178 Å). The scanning $2\theta$ range was 15–85° and the scanning speed was 15° $min^{-1}$.

**Raman measurements.** Raman spectra were measured on a LabRAM HR Evolution Raman spectrometer (Horiba Jobin Yvon), with the range from 200 to 1000 $cm^{-1}$ in a spectral resolution of 1 $cm^{-1}$ (532 nm excitation laser).

**XPS measurements.** X-ray photoelectron spectroscopy (XPS) measurements were conducted on an ESCALAB 250 (Thermo-VG Scientific, USA). An Al $K_\alpha$ X-ray source (1,486.6 eV) in Constant Analyzer Energy (CAE) mode with a pass energy of 30 eV was applied for all spectra. The values of binding energies were calibrated with the C 1*s* peak of contaminant carbon at 284.8 eV.

**XAFS measurements.** The X-ray absorption fine structure (XAFS) measurements were carried out at the 1W1B station at the Beijing Synchrotron Radiation Facility (BSRF). Pt foil and $PtO_2$ spectra were recorded in transmission mode using an ionization chamber. The Pt $L_{III}$-edge spectra of the samples were collected in fluorescent mode. Data processing was based on procedures using ATHENA in the Demeter 0.9.25 software package.

**CO pulse chemisorption experiments.** CO pulse chemisorption experiments were conducted on a Micromeritics AutoChem II 2920 instrument. The $Pt_1/CeO_2$ sample (100 mg) was pretreated in 20% $O_2$/Ar with a total flow rate of 30 mL $min^{-1}$ at 300 °C for 1 h. The $Pt_{CL}/CeO_2$ and $Pt_{NP}/CeO_2$ samples were pretreated in 10% $H_2$/Ar with a total flow rate of 50 mL $min^{-1}$ at 300 °C for 1 h before measurement, followed by cooling down to 50 °C and purging with He for 0.5 h. Subsequently, the sample was purged in He, 20% $O_2$/Ar, 10% $CO_2$/He, and 10% $H_2$/Ar sequentially with a flow rate of 70 mL $min^{-1}$ for 5 min. The catalysts (100 mg) were then treated in He at 50 °C with a flow rate of 70 mL $min^{-1}$ for 20 min before measurement. After cooling down to 50 °C for 1 h, 10% CO/Ar was repeatedly introduced into the reactor until the CO adsorption was saturated. The loop volume was 0.450 mL.

***In situ*-DRIFTS measurements.** The diffuse reflectance infrared Fourier transform spectroscopy (DRIFTS) measurements were accomplished on Thermo Scientific Nicolet iS50 with a resolution of 8 $cm^{-1}$ equipped with an *in-situ* cell (HT-DRIFTS-800) from Beijing Scistar Technology Co. Ltd. Before *in situ*-DRIFTS measurements, the $Pt_1/CeO_2$ sample was pretreated in 20% $O_2$/Ar with a total flow rate of 30 mL $min^{-1}$ at 300 °C for 1 h. The $Pt_{CL}/CeO_2$ and $Pt_{NP}/CeO_2$ samples were treated in He with a total flow rate of 30 mL $min^{-1}$ at 300 °C for 1 h. Each sample was cooled down to 180 °C. Subsequently, the sample was purged in He with a flow rate of 30 mL $min^{-1}$ for 0.5 h. The spectrum was recorded as the background. 30 mL $min^{-1}$ of 1% CO/4% $O_2$ stream was fed to the cell for 20 min. The adsorption spectra were then collected every 60 seconds. Followed by He purge at a flow rate of 30 mL $min^{-1}$, the desorption spectra were recorded every 60 seconds.

**Evaluation of the catalytic performance**

CO oxidation activity was tested using a fixed-bed reactor (d = 0.5 cm). The catalysts (60 mg) were loaded in a quartz tube

and pre-treated with 8% $O_2$/Ar or 10% $H_2$/Ar at 300 °C for 0.5 h. A 1% CO/4% $O_2$ stream was balanced with Ar (20 mL $min^{-1}$) and fed into the reactor. The total gas hourly space velocity (GHSV) was 100 L $g_{cat}^{-1}$ $h^{-1}$. The reactor was heated from 30 °C to 300 °C (2 °C $min^{-1}$). All the outlet gases were analyzed online by the Gasboard-3100 flue gas analyzer (Cubic Instruments). The CO conversion was derived from the equation:

$$CO_{conversion} = CO_{converted} / CO_{input}$$

The cycling catalytic stability was examined by continuously performing activity tests 5 times (GHSV = 100 L $g_{cat}^{-1}$ $h^{-1}$). The apparent activation energy ($E_a$) and reaction order were obtained by regulating the reaction temperature, gas flow rate, gas ratio, and the loading of the catalysts within the kinetic region. The reaction rates ($r$) of the catalysts were calculated with the expression below:

$$r = F \times CO_{converted}/W, (\mu mol\ g_{cat}^{-1}\ s^{-1})$$

where $F$, $CO_{converted}$, and W refer to the gas flow rate (mol $s^{-1}$), the converted CO concentration and the catalyst mass (g), respectively.

The turnover frequency (TOF) was calculated with the expression below:

$$TOF = r \times M/(10^6 \times w \times D), (s^{-1})$$

where M, w, and D refer to the molar mass of Pt (g $mol^{-1}$), loading of Pt and the dispersion of Pt, respectively.

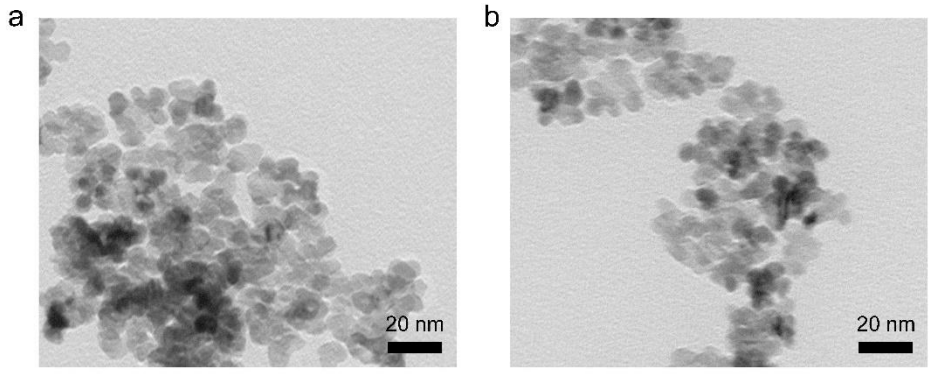


**Figure S1** (**a**, **b**) TEM images of the $CeO_2$ support.

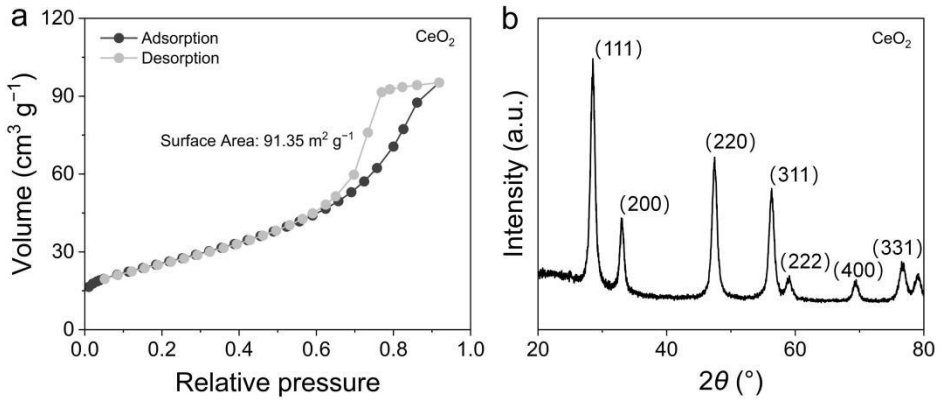


**Figure S2** (**a**) Nitrogen adsorption isotherm and surface area of the $CeO_2$ support. (**b**) XRD pattern of the $CeO_2$ support.

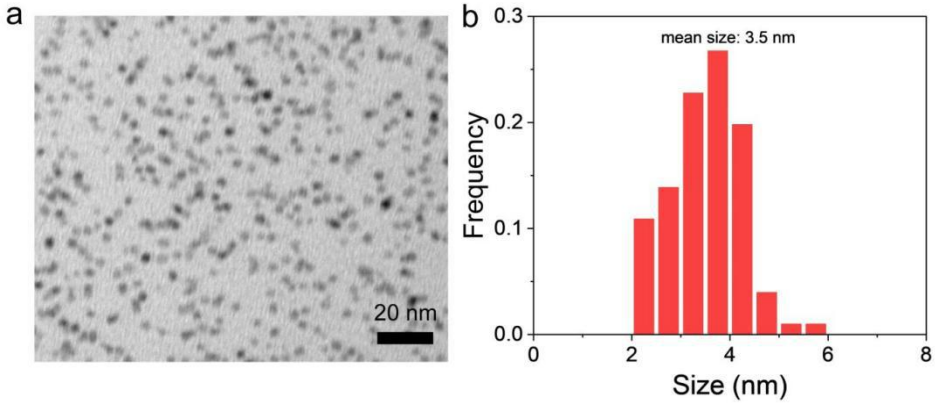


**Figure S3** (**a**) TEM images of Pt nanoparticles. (**b**) Size distribution of Pt nanoparticles.

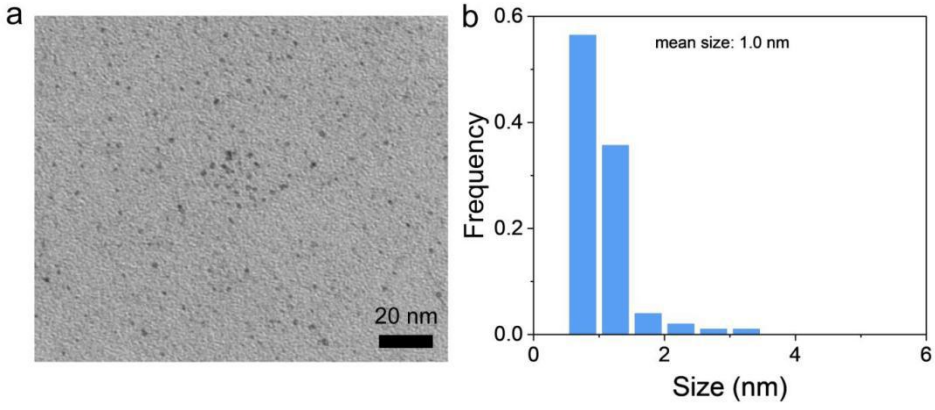


**Figure S4** (**a**) TEM images of Pt nanoclusters. (**b**) Size distribution of Pt nanoclusters.

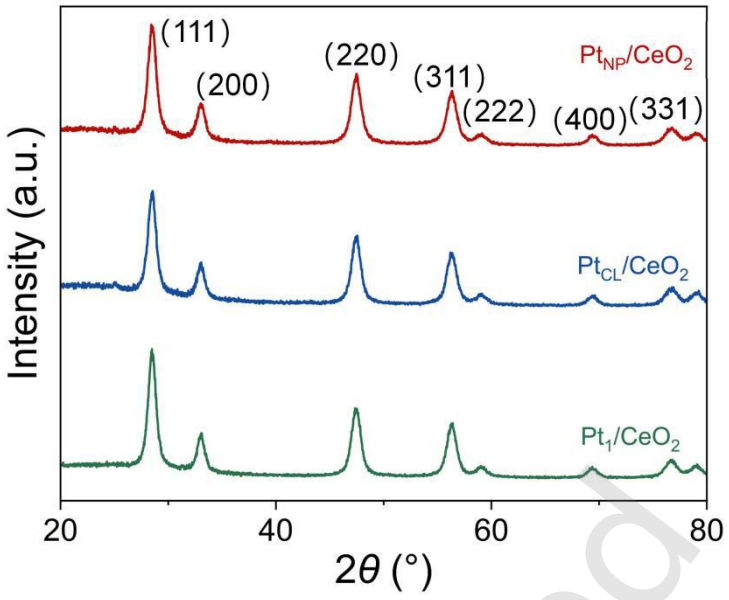


**Figure S5** XRD patterns of $Pt_{NP}/CeO_2$, $Pt_{CL}/CeO_2$, and $Pt_1/CeO_2$ catalysts.

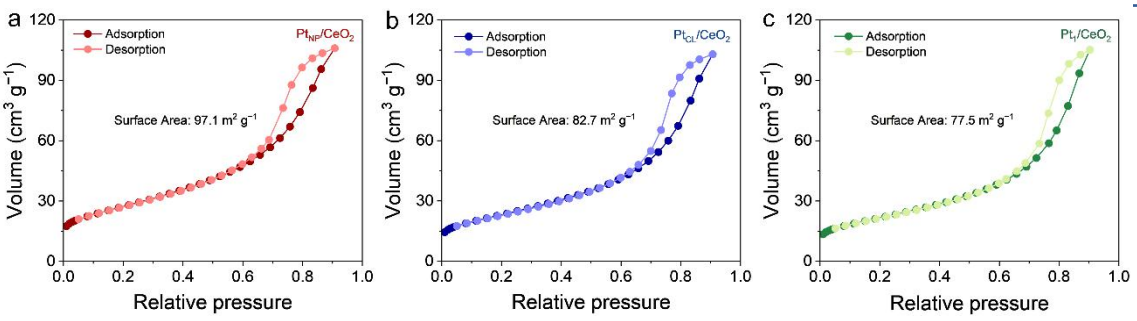


**Figure S6** (**a**–**c**) Nitrogen adsorption isotherms and surface areas of $Pt_{NP}/CeO_2$, $Pt_{CL}/CeO_2$, and $Pt_1/CeO_2$ catalysts.

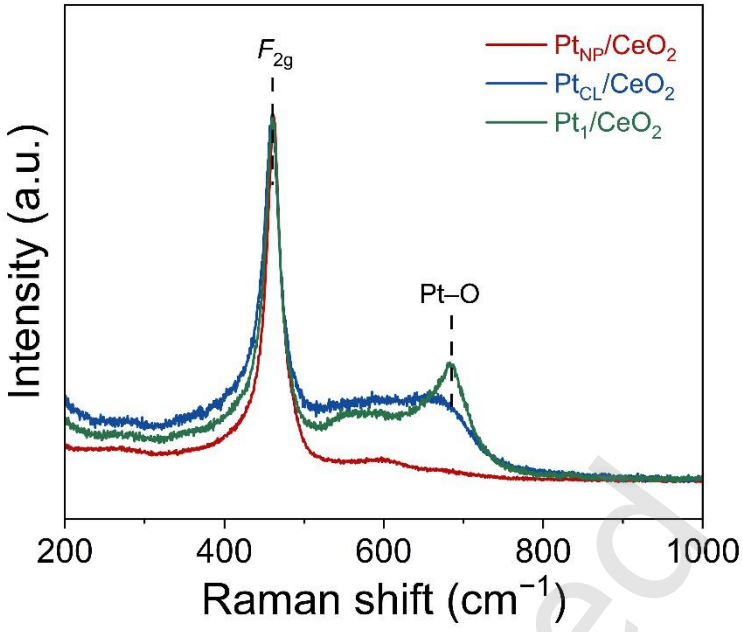


**Figure S7** Raman spectra of $Pt_{NP}/CeO_2$, $Pt_{CL}/CeO_2$, and $Pt_1/CeO_2$ catalysts.

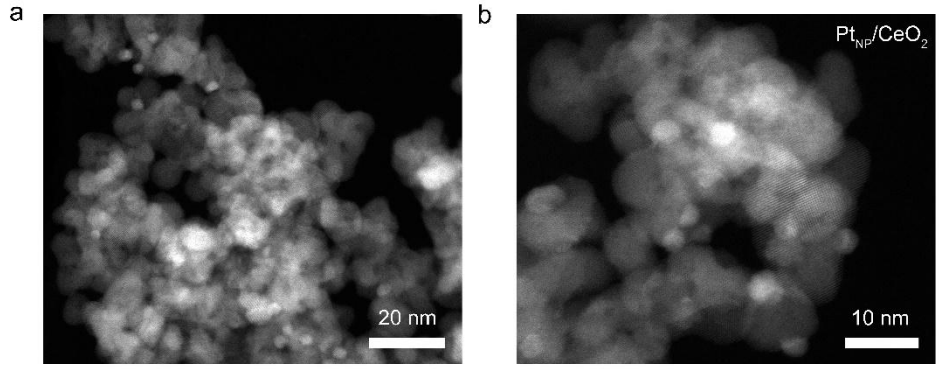


**Figure S8** (**a, b**) AC-HAADF-STEM images of $Pt_{NP}/CeO_2$ with low magnifications.

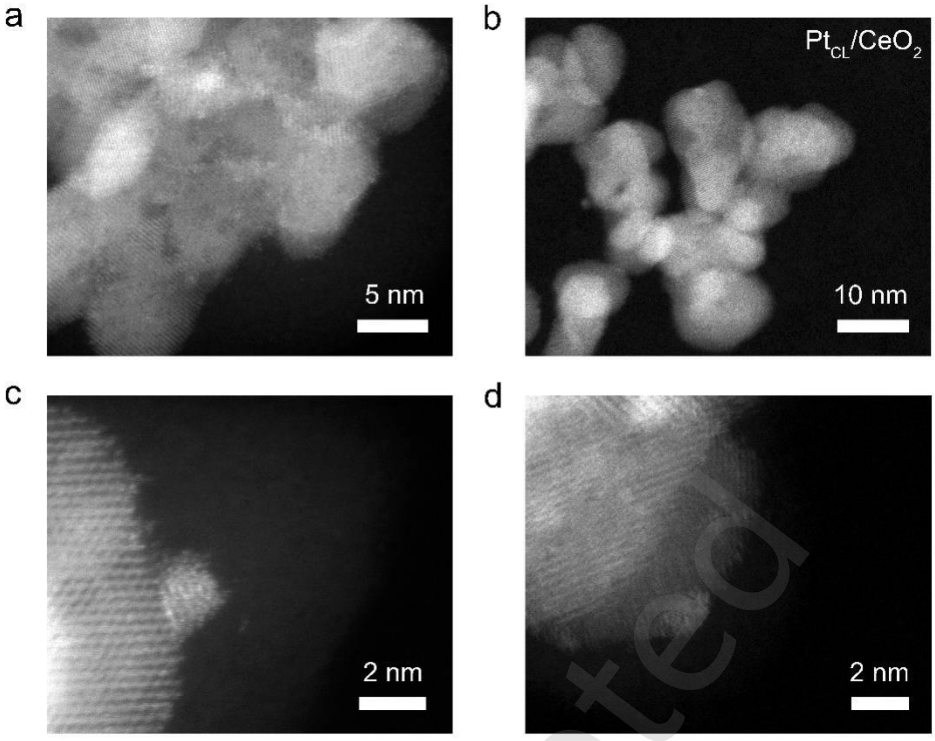


**Figure S9 (a–d)** AC-HAADF-STEM images of $Pt_{CL}/CeO_2$ with low and high magnifications.

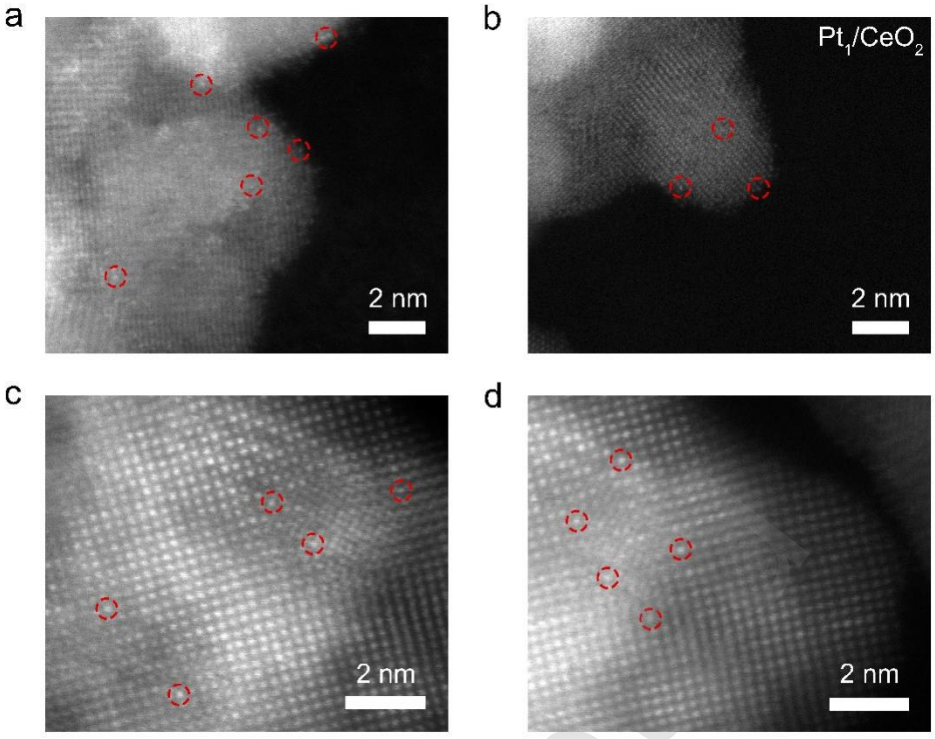


**Figure S10** (**a–d**) AC-HAADF-STEM images of $Pt_1/CeO_2$ with high magnifications.

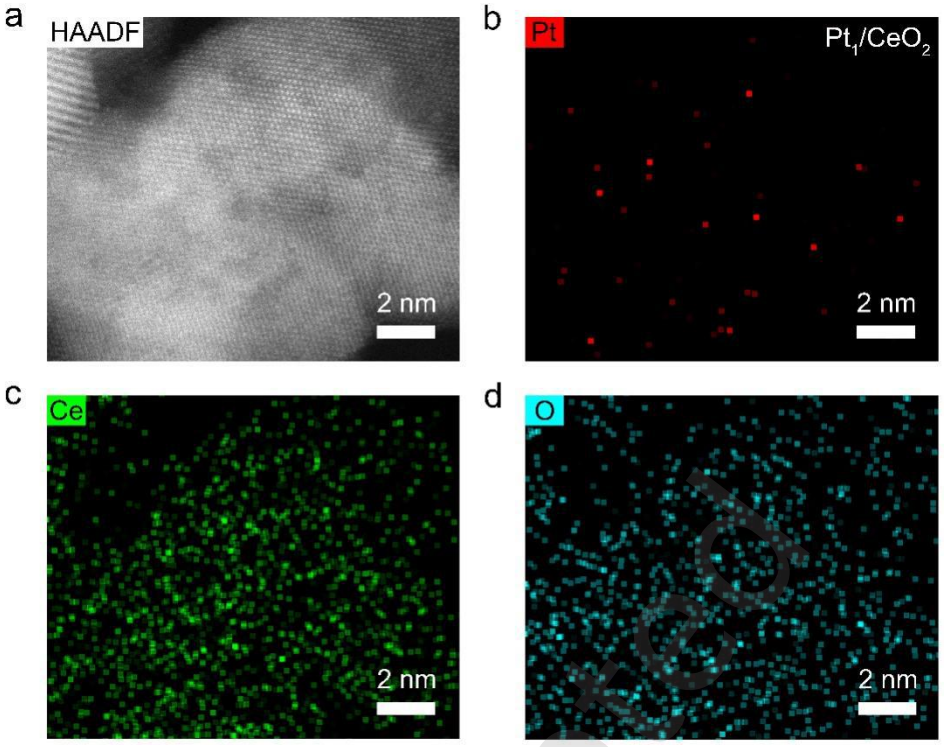


**Figure S11 (a–d)** Elemental mapping results of $Pt_1/CeO_2$.

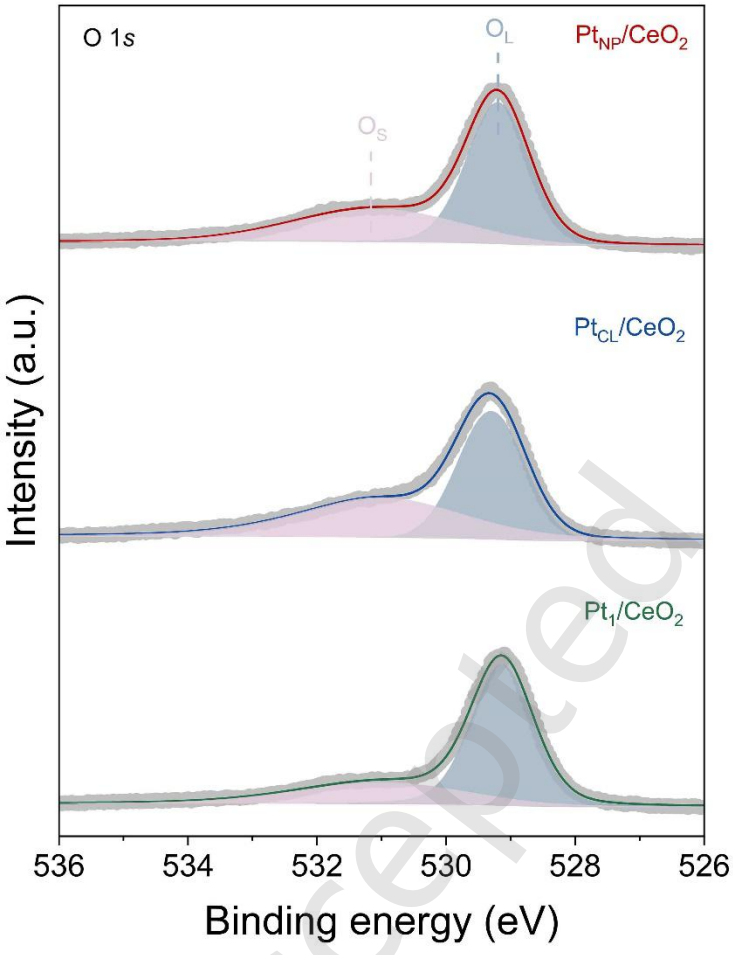


**Figure S12** O 1*s* XPS results of $Pt_{NP}/CeO_2$, $Pt_{CL}/CeO_2$, and $Pt_1/CeO_2$ catalysts.

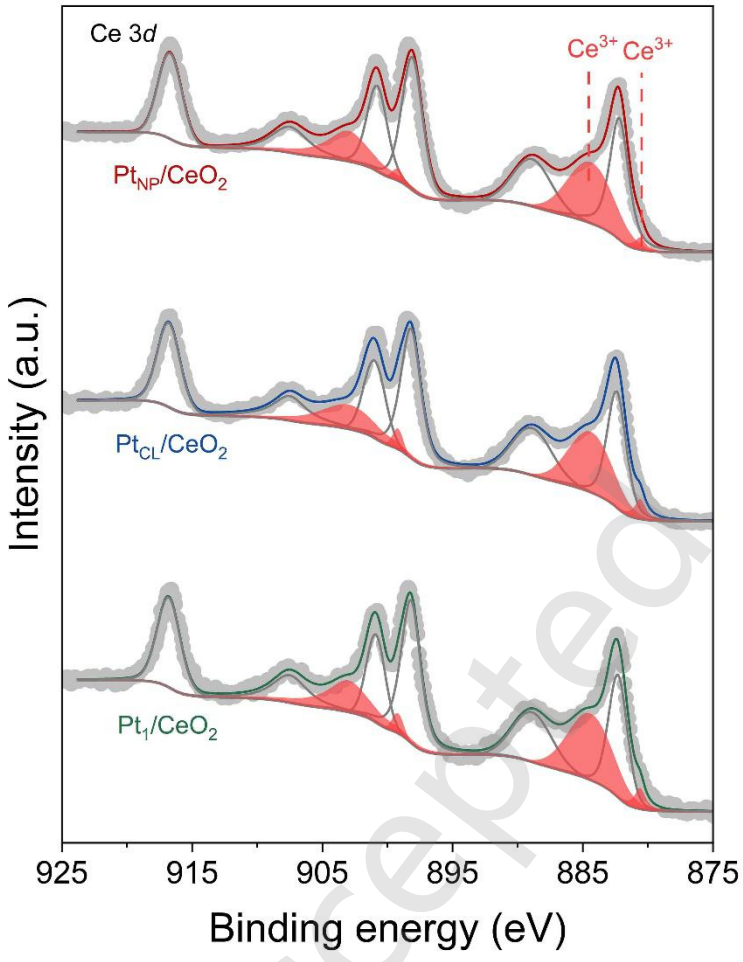


**Figure S13** Ce 3*d* XPS results of $Pt_{NP}/CeO_2$, $Pt_{CL}/CeO_2$, and $Pt_1/CeO_2$ catalysts.

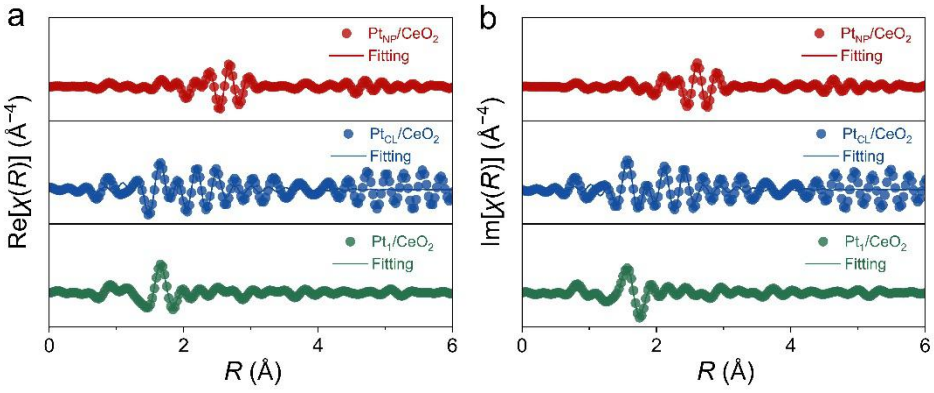


**Figure S14** EXAFS fitting curves of (**a**) the real part, and (**b**) imaginary part for $Pt_{NP}/CeO_2$, $Pt_{CL}/CeO_2$, and $Pt_1/CeO_2$ catalysts.

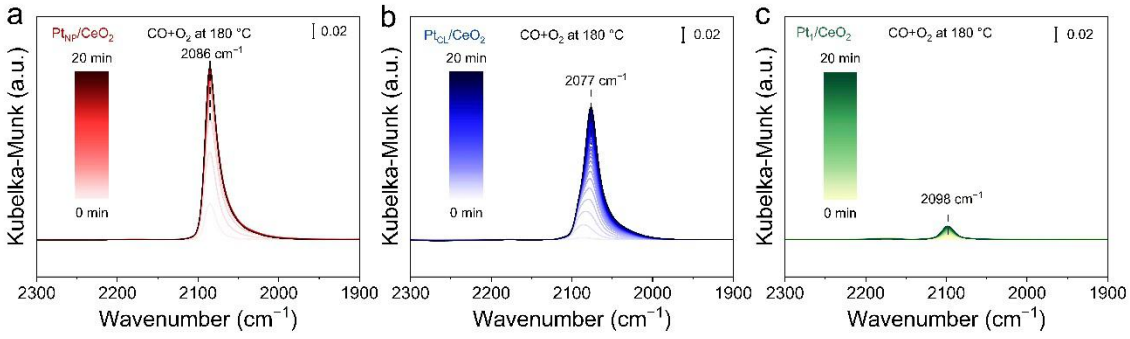


**Figure S15** (**a**–**c**) Adsorption mode of *in situ*-DRIFTS for $Pt_{NP}/CeO_2$, $Pt_{CL}/CeO_2$, and $Pt_1/CeO_2$ catalysts.

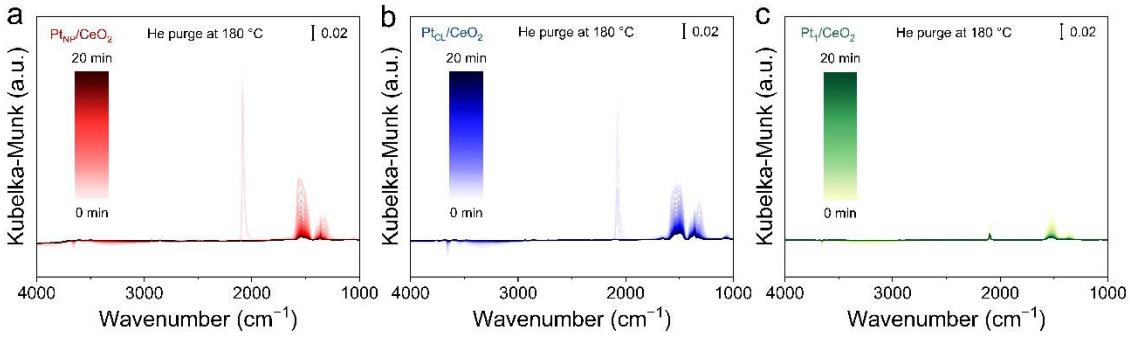


**Figure S16** (**a**–**c**) Desorption mode of *in situ*-DRIFTS for $Pt_{NP}/CeO_2$, $Pt_{CL}/CeO_2$, and $Pt_1/CeO_2$ catalysts.

**Table S1** Curve-fit parameters for Pt $L_{III}$-edge EXAFS of $Pt/CeO_2$ samples.

| Samples | Path | CN[a] | $R$ (Å)[b] | $\sigma^{2}$[c] | $\Delta E_0$ (eV)[d] | R-factor |
|---|---|---|---|---|---|---|
| $Pt_{NP}/CeO_2$ | Pt–O | 1.2±0.5 | 1.99±0.03 | 0.007 | 9.9 | 0.016 |
| | Pt–Pt | 7.1±1.1 | 2.75±0.01 | 0.006 | 7.1 | |
| $Pt_{CL}/CeO_2$ | Pt–O | 3.3±0.9 | 1.96±0.02 | 0.004 | 5.2 | 0.046 |
| | Pt–Pt | 1.7±0.8 | 2.53±0.05 | 0.004 | 0.7 | |
| $Pt_1/CeO_2$ | Pt–O | 5.5±0.7 | 1.99±0.01 | 0.003 | 13.5 | 0.018 |

[a]CN, coordination numbers;

[b]$R$, bonding distance;

[c]$\sigma^2$, Debye-Waller factor;

[d]$\Delta E_0$, inner potential shift.